

Laboratory Determination of Thermal Protection System Materials Surface Catalytic Properties

Jochen Marschall

Molecular Physics Laboratory, SRI International
333 Ravenswood Avenue
Menlo Park, CA 94025
USA

jochen.marschall@sri.com

ABSTRACT

Different experimental approaches to measuring catalytic reaction efficiencies on thermal protection system materials are reviewed. Special emphasis is given to the theory and application of the diffusion tube side-arm reactor technique. In this technique, reactants diffuse into a dead-end tube and are progressively removed from the gas phase by surface reactions on the walls, establishing unique steady-state concentration profiles along the length of the tube. Reactant loss probabilities are determined by matching experimentally measured species profiles to calculated solutions of a reaction-diffusion model. The advantages of laser-based methods for species concentration measurements are summarized and different approaches to reactor modeling and the extraction of reaction efficiencies from measured data are presented. The advantages and limitations of the diffusion-tube side-arm technique, the associated uncertainties in derived loss probabilities, and the prospects for further laboratory development, are presented.

1.0 INTRODUCTION

During hypersonic flight through a planetary atmosphere, shock waves form as gases are rapidly compressed ahead of leading surfaces. High energy intermolecular collisions within the shock layer heat the gas and cause molecular species to dissociate. The extent of molecular dissociation depends on many factors, including the atmospheric composition and the vehicle shape, velocity, and altitude. Dissociated gas species can diffuse through the boundary layer to the vehicle surface, where they have the potential to undergo exothermic surface-catalyzed recombination reactions. Some fraction of the energy liberated by recombination may be transferred directly to the vehicle surface as heat. The greater the extent of dissociation and the more efficient the surface is at catalyzing recombination reactions, the more likely it is that recombination contributes significantly to the total aerothermodynamic heat load.

Oxygen and nitrogen molecules are the relevant species in the Earth's atmosphere. Oxygen is more easily dissociated than nitrogen, since it has a lower dissociation energy (~5.1 eV compared to ~9.8 eV.) The importance of surface catalyzed reactions to Earth re-entry heating was demonstrated in a series of flight experiments on the Space Shuttle Orbiter.¹⁻³ Adjacent thermal protection system (TPS) tiles in the base heat shield of the orbiter attained significantly different surface temperatures depending on the catalytic efficiency of their surface coating.

Marschall, J. (2007) Laboratory Determination of Thermal Protection System Materials Surface Catalytic Properties. In *Experiment, Modeling and Simulation of Gas-Surface Interactions for Reactive Flows in Hypersonic Flights* (pp. 11-1 – 11-32). Educational Notes RTO-EN-AVT-142, Paper 11. Neuilly-sur-Seine, France: RTO. Available from: <http://www.rto.nato.int/abstracts.asp>.

Report Documentation Page				Form Approved OMB No. 0704-0188	
Public reporting burden for the collection of information is estimated to average 1 hour per response, including the time for reviewing instructions, searching existing data sources, gathering and maintaining the data needed, and completing and reviewing the collection of information. Send comments regarding this burden estimate or any other aspect of this collection of information, including suggestions for reducing this burden, to Washington Headquarters Services, Directorate for Information Operations and Reports, 1215 Jefferson Davis Highway, Suite 1204, Arlington VA 22202-4302. Respondents should be aware that notwithstanding any other provision of law, no person shall be subject to a penalty for failing to comply with a collection of information if it does not display a currently valid OMB control number.					
1. REPORT DATE 01 JUL 2007		2. REPORT TYPE N/A		3. DATES COVERED -	
4. TITLE AND SUBTITLE Laboratory Determination of Thermal Protection System Materials Surface Catalytic Properties				5a. CONTRACT NUMBER	
				5b. GRANT NUMBER	
				5c. PROGRAM ELEMENT NUMBER	
6. AUTHOR(S)				5d. PROJECT NUMBER	
				5e. TASK NUMBER	
				5f. WORK UNIT NUMBER	
7. PERFORMING ORGANIZATION NAME(S) AND ADDRESS(ES) Molecular Physics Laboratory, SRI International 333 Ravenswood Avenue Menlo Park, CA 94025 USA				8. PERFORMING ORGANIZATION REPORT NUMBER	
9. SPONSORING/MONITORING AGENCY NAME(S) AND ADDRESS(ES)				10. SPONSOR/MONITOR'S ACRONYM(S)	
				11. SPONSOR/MONITOR'S REPORT NUMBER(S)	
12. DISTRIBUTION/AVAILABILITY STATEMENT Approved for public release, distribution unlimited					
13. SUPPLEMENTARY NOTES See also ADM002058., The original document contains color images.					
14. ABSTRACT					
15. SUBJECT TERMS					
16. SECURITY CLASSIFICATION OF:			17. LIMITATION OF ABSTRACT UU	18. NUMBER OF PAGES 32	19a. NAME OF RESPONSIBLE PERSON
a. REPORT unclassified	b. ABSTRACT unclassified	c. THIS PAGE unclassified			

During high speed entry into extraterrestrial atmospheres, the dissociation and recombination of other species can be important. For example, the dissociation of CO_2 during Martian entries enables the surface reactions $\text{CO} + \text{O}$ and $\text{O} + \text{O}$, and the dissociation of methane during Titan entries creates atomic hydrogen for heterogeneous $\text{H} + \text{H}$ recombination.

The quantity of heat transferred to a catalytic surface by a particular recombination reaction pathway depends first on the efficiency of surface in catalyzing the reaction, and second, on the efficiency of the energy transfer process between the energetic product molecules and the surface. Since surface reaction must precede energy transfer, reaction efficiency is the more globally important parameter. It is also more experimentally accessible, although by no means straightforward to determine.

Neither reaction nor energy transfer efficiencies can be measured directly. Experiments must probe the effects of surface reactions on the gas phase concentrations of reactants or products near catalytic surfaces or the flow of heat to catalytic bodies. Measurements of the latter phenomenon are generally insufficient to separate reaction and energy transfer efficiencies without additional assumptions or information, whereas species concentration data can be related much more directly to reaction efficiencies through appropriate chemical and transport models.

Experiments to determine catalytic efficiencies for TPS materials can be divided into two categories: measurements in high enthalpy facilities such as arc-jets, induction plasmatrons, and shock tubes, and measurements in low enthalpy laboratory systems such as diffusion tubes or flow tubes. The former more closely reproduce aspects of the flow environments seen during hypersonic flight, but are also much more complicated to operate and generally generate temperature or heat flux data. In contrast, laboratory systems are more amenable to controlled and well-characterized experiments, although under conditions far from those in flight.

In this lecture, laboratory approaches for determining catalytic efficiencies are discussed, with a specific focus on the diffusion-tube side-arm reactor technique in combination with laser-based species detection diagnostics.

2.0 SURFACE CATALYSIS: DEFINITIONS AND MODELS

2.1 Basic Quantities

We consider heterogeneous chemical reactions mediated by adsorption of one or more reactants on the surface of a TPS material. Discussion is limited to chemical reactions in which the TPS material is not consumed or converted. The TPS material participates by providing an environment for the reaction of impinging gas phase species, and acts as a *catalytic* surface when it enhances the net rate of a thermodynamically-favoured chemical reaction. The catalytic characteristics of a surface for a particular reaction can range between two limits. When the reaction rate is negligible the surface is said to be *non-catalytic*; when the reaction proceeds at the maximum possible rate the surface is termed *fully-catalytic*.

The net production of species i by surface-catalyzed reactions must be balanced by its net diffusive flux $J_{i,w}$ at the wall. For a one-dimensional body-fitted coordinate system

$$J_{i,w} = -D_i \left. \frac{\partial n_i}{\partial z} \right|_w = \dot{w}_i, \quad (1)$$

where z is the normal coordinate to the wall (positive outward), n_i is the number density, D_i is the diffusion coefficient, and \dot{w}_i is the net species production rate (positive for formation, negative for consumption).

For *reactant* species it is often convenient to express the net flux to the surface in terms of a *loss probability*, γ_i , times the *surface impingement flux*, Γ_i . Then the production rate of the reactant at the surface is

$$\dot{w}_i = -\gamma_i \Gamma_i. \quad (2)$$

The impingement flux is typically approximated by the classic gas kinetic expression

$$\Gamma_i = n_{i,w} \frac{\bar{v}_i}{4}, \quad (3)$$

with $n_{i,w}$ the species concentration at the wall and \bar{v}_i the average thermal speed given by

$$\bar{v}_i = \sqrt{\frac{8\Re T}{\pi M_i}}, \quad (4)$$

where \Re is the universal gas constant; T is the temperature, and M_i is the molar mass of the species.

The loss probability is defined here as *the fraction of impinging reactant flux removed permanently from the gas phase*. With this definition, the loss probability is equivalent to the “uptake coefficient” found in the atmospheric heterogeneous chemistry literature. For atom recombination via a single reaction pathway, the loss probability is often called the “recombination coefficient.”

It is important to remember that γ_i is not uniquely associated with a single chemical process in the same way that a reaction rate coefficient is associated with a specific gas phase reaction. Rather, γ_i reflects the total efficiency of all operating surface reaction pathways that remove species i on a particular surface under a particular combination of temperature, pressure, and gas composition. Similar to other surface properties like emittance and reflectance, the loss probability depends both on the chemical nature and the microscopic geometric characteristics of the surface. The absolute lower and upper bounds on γ_i are 0 and 1, but this range may be limited further by various other factors such as the availability of partner reactants or free reaction sites on the surface.

2.2 Element Conservation

Element conservation is the most basic physical constraint on numerical values of loss probabilities. Element conservation also ensures mass conservation. For a single reactant participating in a single recombination reaction, element conservation is consistent with the 0 through 1 range of loss probability. However, when a reactant participates in more than one surface reaction or when surface reactions involve two different reactant species, element conservation can constrain the range further.

Consider a partially dissociated mixture of oxygen and nitrogen interacting with a catalytic surface via three net steady-state heterogeneous reaction pathways: $O + O \rightarrow O_2$, $N + N \rightarrow N_2$, and $O + N \rightarrow NO$. Element conservation dictates

$$\dot{w}_{NO} + 2\dot{w}_{O_2} + \dot{w}_O = 0 \quad (5)$$

$$\dot{w}_{NO} + 2\dot{w}_{N_2} + \dot{w}_N = 0 \quad (6)$$

The production rate of nitric oxide can be eliminated from this equation set, and with some rearrangement the relation

$$\gamma_O \Gamma_O (1 - f_{O_2}) = \gamma_N \Gamma_N (1 - f_{N_2}) \quad (7)$$

is obtained, where f_{O_2} is defined as $-2\dot{w}_{O_2}/\dot{w}_O$, the fraction of the total O-atom loss that forms O_2 , and f_{N_2} is defined as $-2\dot{w}_{N_2}/\dot{w}_N$, the fraction of the total N-atom loss that forms N_2 . By definition the four parameters γ_O , γ_N , f_{O_2} , and f_{N_2} can be no smaller than zero and no larger than one, however all four values cannot be specified independently because they must also be consistent with Eq. 7.

For any allowed set of parameters, the individual production rates are then

$$\dot{w}_O = -\gamma_O \Gamma_O \quad (8a)$$

$$\dot{w}_N = -\gamma_N \Gamma_N \quad (8b)$$

$$\dot{w}_{O_2} = f_{O_2} \frac{\gamma_O}{2} \Gamma_O \quad (8c)$$

$$\dot{w}_{N_2} = f_{N_2} \frac{\gamma_N}{2} \Gamma_N \quad (8d)$$

$$\dot{w}_{NO} = \gamma_O \Gamma_O (1 - f_{O_2}) = \gamma_N \Gamma_N (1 - f_{N_2}) \quad (8e)$$

2.3 Surface Reaction Models

Element conservation is a necessary condition for a physically consistent description of surface catalytic effects, but it does not directly relate loss probabilities to chemical mechanisms on the surface. A surface chemistry model is required to link net species production rates to a specific set of finite-rate surface reactions and their dependencies on gas composition, temperature, and active site density (or reactive surface area).

The “true” chemical processes that take place at a catalytic surface are extremely complex, even for simple reactions on pristine surfaces.⁴ A phenomenological mechanistic description of the temperature and compositional dependencies of the dominant kinetic processes suffices in many chemical engineering applications; this approach has been applied in various forms to describe surface catalysis for aerothermal computations, primarily in the European aerospace community.⁵⁻⁸

Table 1: Surface Reaction Model for O-O₂-N-N₂-NO system

Reaction	Site Filling Flux (moles m ⁻² s ⁻¹)
Adsorption	
R1 O + [s] → O _s	$S_o \theta \Gamma_o$
R2 N + [s] → N _s	$S_N \theta \Gamma_N$
Thermal Desorption	
R3 O _s → O + [s]	$-\nu_{D,O} \theta_o \Phi_s$
R4 N _s → N + [s]	$-\nu_{D,N} \theta_N \Phi_s$
Eley-Rideal Recombination	
R5 O + O _s → O ₂ + [s]	$-\gamma_{ER,OO} \theta_o \Gamma_o$
R6 N + N _s → N ₂ + [s]	$-\gamma_{ER,NN} \theta_N \Gamma_N$
R7 O + N _s → NO + [s]	$-\gamma_{ER,ON} \theta_N \Gamma_o$
R8 N + O _s → NO + [s]	$-\gamma_{ER,NO} \theta_o \Gamma_N$
Langmuir-Hinshelwood Recombination	
R9 O _{s,m} + O _s → O ₂ + 2[s]	$-2\nu_{LH,OO} \theta_o^2 \Phi_s$
R10 N _{s,m} + N _s → N ₂ + 2[s]	$-2\nu_{LH,NN} \theta_N^2 \Phi_s$
R11 O _{s,m} + N _s → NO + 2[s]	$-2\nu_{LH,ON} \theta_o \theta_N \Phi_s$
R12 N _{s,m} + O _s → NO + 2[s]	$-2\nu_{LH,NO} \theta_N \theta_o \Phi_s$
Variables	
Φ_s	Active site density, (moles m ⁻²)
θ, θ_i	Fraction of active sites, free or occupied by species <i>i</i>
S_i	Sticking coefficient for species <i>i</i>
$\nu_{D,i}$	Thermal desorption frequency for species <i>i</i> , (s ⁻¹)
$\gamma_{ER,ij}$	Eley-Rideal reaction efficiency between gas phase species <i>i</i> and adsorbed species <i>j</i>
$\nu_{LH,ij}$	Langmuir-Hinshelwood reaction frequency between mobile species <i>i</i> and immobile species <i>j</i> , (s ⁻¹)

For the partially-dissociated oxygen-nitrogen system, a simple finite-rate surface reaction model can be constructed based on two reactants (O and N atoms) and the four kinetic processes of adsorption, thermal desorption, Eley-Rideal (ER) recombination, and Langmuir-Hinshelwood (LH) recombination. All processes for both reactants are envisioned to take place at a finite number of identical active sites, [s], on the surface.

ER recombination occurs between an adsorbed atom and an impinging gas phase atom; LH recombination occurs between two adsorbed atoms, one of which is mobile. In both types of recombination, the product molecule is assumed to desorb instantaneously. The reverse processes of dissociative O₂, N₂, and NO adsorption are not included.

Table 1 lists the individual reactions and corresponding expressions for the active site filling fluxes, as well as the variable definitions.

At steady-state, the number of active sites occupied by each atomic species is constant and the site filling fluxes must sum to zero:

$$\Phi_s \frac{d\theta_o}{dt} = 0 = S_o \theta \Gamma_o - \nu_{D,O} \theta_o \Phi_s - \gamma_{ER,OO} \theta_o \Gamma_o - \gamma_{ER,NO} \theta_o \Gamma_N - 2\nu_{LH,OO} \theta_o^2 \Phi_s - \nu_{LH,NO} \theta_N \theta_o \Phi_s - \nu_{LH,ON} \theta_o \theta_N \Phi_s \quad (9)$$

$$\Phi_s \frac{d\theta_N}{dt} = 0 = S_N \theta \Gamma_N - \nu_{D,N} \theta_N \Phi_s - \gamma_{ER,NN} \theta_N \Gamma_N - \gamma_{ER,ON} \theta_N \Gamma_o - 2\nu_{LH,NN} \theta_N^2 \Phi_s - \nu_{LH,ON} \theta_o \theta_N \Phi_s - \nu_{LH,NO} \theta_N \theta_o \Phi_s \quad (10)$$

From these relations and the identity $\theta = 1 - \theta_o - \theta_N$, the fractional surface coverage of each atomic species can be obtained from the coupled quadratic equations:

$$a_o \theta_o^2 + b_o \theta_o + c_o = 0 \quad (11a)$$

$$a_N \theta_N^2 + b_N \theta_N + c_N = 0, \quad (11b)$$

with

$$a_o = 2\nu_{LH,OO} \Phi_s, \quad b_o = \nu_{D,O} \Phi_s + \gamma_{ER,OO} \Gamma_o + \gamma_{ER,NO} \Gamma_N + (\nu_{LH,NO} + \nu_{LH,ON}) \theta_N \Phi_s + S_o \Gamma_o, \quad c_o = S_o \Gamma_o (\theta_N - 1) \quad (12a)$$

$$a_N = 2\nu_{LH,NN} \Phi_s, \quad b_N = \nu_{D,N} \Phi_s + \gamma_{ER,NN} \Gamma_N + \gamma_{ER,ON} \Gamma_o + (\nu_{LH,ON} + \nu_{LH,NO}) \theta_o \Phi_s + S_N \Gamma_N, \quad c_N = S_N \Gamma_N (\theta_o - 1) \quad (12b)$$

Expressions for the species production rates are

$$\dot{w}_o = -S_o \theta \Gamma_o + \nu_{D,O} \theta_o \Phi_s - \gamma_{ER,OO} \theta_o \Gamma_o - \gamma_{ER,ON} \theta_N \Gamma_o \quad (13a)$$

$$\dot{w}_N = -S_N \theta \Gamma_N + \nu_{D,N} \theta_N \Phi_s - \gamma_{ER,NN} \theta_N \Gamma_N - \gamma_{ER,NO} \theta_o \Gamma_N \quad (13b)$$

$$\dot{w}_{O_2} = \gamma_{ER,OO} \theta_o \Gamma_o + \nu_{LH,OO} \theta_o^2 \Phi_s \quad (13c)$$

$$\dot{w}_{N_2} = \gamma_{ER,NN} \theta_N \Gamma_N + \nu_{LH,NN} \theta_N^2 \Phi_s \quad (13d)$$

$$\dot{w}_{NO} = \gamma_{ER,ON} \theta_N \Gamma_o + \gamma_{ER,NO} \theta_o \Gamma_N + \nu_{LH,ON} \theta_o \theta_N \Phi_s + \nu_{LH,NO} \theta_N \theta_o \Phi_s \quad (13e)$$

and expressions for the atom loss probabilities follow directly from Eq. 2:

$$\gamma_o = S_o \theta + \gamma_{ER,OO} \theta_o + \gamma_{ER,ON} \theta_N - \frac{\nu_{D,O} \theta_o \Phi_s}{\Gamma_o} \quad (14a)$$

$$\gamma_N = S_N \theta + \gamma_{ER,NN} \theta_N + \gamma_{ER,NO} \theta_o - \frac{\nu_{D,N} \theta_N \Phi_s}{\Gamma_N} \quad (14b)$$

This simple surface reaction model illustrates the complexity in systems of coupled heterogeneous reactions. The loss probability of each individual atomic species is dependent on the availability of both species and their individual chemical interactions with the surface.

The complexity of the model can be methodically reduced by eliminating certain interactions. For example, the assumptions that NO is not produced heterogeneously and that O + O and N + N recombination proceed on independent sets of active surface sites, $\Phi_{s,O}$ and $\Phi_{s,N}$, decouples the oxygen and nitrogen chemistry. So for oxygen,

$$a_o = 2\nu_{LH,OO} \Phi_{s,O}, \quad b_o = \nu_{D,O} \Phi_{s,O} + \gamma_{ER,OO} \Gamma_o + S_o \Gamma_o, \quad c_o = -S_o \Gamma_o \quad (15)$$

$$\dot{w}_o = -S_o \theta \Gamma_o + \nu_{D,O} \theta_o \Phi_{s,O} - \gamma_{ER,OO} \theta_o \Gamma_o \quad (16)$$

$$\dot{w}_{O_2} = \gamma_{ER,OO} \theta_o \Gamma_o + \nu_{LH,OO} \theta_o^2 \Phi_{s,O} \quad (17)$$

$$\gamma_o = S_o \theta + \gamma_{ER,OO} \theta_o - \frac{\nu_{D,O} \theta_o \Phi_{s,O}}{\Gamma_o} \quad (18)$$

with analogous expressions for nitrogen.

Even further simplification is obtained by assuming that thermal desorption is negligible and that only Eley-Rideal processes take place. Then for oxygen we have the very simple relationships,

$$a_o = 0, \quad b_o = \gamma_{ER,OO} \Gamma_o + S_o \Gamma_o, \quad c_o = -S_o \Gamma_o \quad (19)$$

$$\dot{w}_o = -S_o \theta \Gamma_o - \gamma_{ER,OO} \theta_o \Gamma_o \quad (20)$$

$$\dot{w}_{O_2} = \gamma_{ER,OO} \theta_o \Gamma_o \quad (21)$$

$$\gamma_o = \frac{2S_o \gamma_{ER,OO}}{S_o + \gamma_{ER,OO}}, \quad (22)$$

again with symmetric expressions for nitrogen atoms. By their formulation in terms of steady-state species fluxes, all surface reaction models above automatically satisfy element conservation.

2.4 Application to Simulation and Data Analysis

Equation set 8 together with relation 7 can be used to specify species production rates in diffusive flux boundary conditions (Eq. 1), to ensure that numerical simulations of reactive flow interactions with a catalytic surface are *at least* constrained to a parameter space consistent with element (and mass) conservation. The extremes within this parameter space can be used to bound the effects of different surface reaction pathways and their efficiencies on gas composition, catalytic heating rates, etc.

Laboratory experiments investigating catalytic surfaces can involve measurements of species concentrations and concentration gradients near surfaces, since these quantities reflect the species production rates at the surface. Reactive flow simulations can be tuned to match measured data by adjusting loss probabilities in the boundary conditions to obtain the best agreement possible. The resulting values are not fundamental chemical quantities, but rather empirical parameters that relate experimental species production rates to reactant impingement fluxes under specific gas composition, temperature, and pressure conditions.

Analytic fits to experimental loss probabilities are often used in reactive-flow simulations attempting to predict the catalytic effects on heating and gas composition in different flight and test environments. Typically, these fits contain only the temperature dependence of the loss probability, with no information on pressure or gas composition dependencies.⁹⁻¹¹ By using an analytic fit of this sort, the same assumptions required to obtain Eq. 22 are implicitly assumed; i.e., a single atom recombination reaction on an independent sets of active sites, negligible atom desorption, and only ER recombination.

A preferred approach is to use a general surface chemistry model to extrapolate and interpolate loss probabilities. The variables describing the efficiencies or frequencies of the various heterogeneous processes - S_i , $\nu_{D,i}$, $\gamma_{ER,ij}$, and $\nu_{LH,ij}$ - are not constants in general. Analytic formulas for their temperature dependences can be obtained from kinetic and transition state theory, and typically involve Arrhenius-type expressions with temperature-dependent prefactors.^{7,8,12} Thus at least nine quantities – four activation energies, four prefactors, and the active site density, Φ_s , must be assigned numerical values to complete the model in Table 1.

A surface chemistry model can be fit to experimental data by adjusting these model parameters to reproduce experimental results. Experimental data must be available over a sufficiently wide range of pressures, temperatures, and gas compositions, so that model parameters are both robustly determined and retain physically plausible numerical values. Such wide-ranging data sets are rarely available, and in practice, some arbitrary choices must be made, guided by ancillary information in the chemistry and physics literature. Nevertheless, a surface reaction model is a fitting function with a mathematical formulation that can be justified, at least to some extent, by underlying physical and kinetic mechanisms.

3.0 OVERVIEW OF LABORATORY METHODS

Laboratory methods characterizing atom recombination reactions at an “engineering” level have primarily used flow or diffusion tube reactors, in conjunction with different methods of generating reactants, measuring species concentrations, and extracting numerical values for loss probabilities. Experiments in these reactors involve spatially resolved reactant concentration measurements in the vicinity of a catalytic specimen and/or energy transfer measurements to a catalytic sample or probe. Smith¹³ first introduced the diffusion-tube side-arm reactor design in 1943 to study surface reactions on materials of low catalytic efficiency. One of the primary advantages of the diffusion tube approach is that species transport is greatly simplified, and complications associated with measuring and modelling the interactions of different convective and diffusive flow regimes are avoided.

A great deal of work was performed in both types of reactor systems from the late 1950’s through the early 1970’s, including frequently cited works by Melin and Madix^{14,15}, Linnett *et al.*¹⁶⁻²⁴, and Wise, Wood and coworkers.²⁵⁻⁴⁰ Atoms were generated using a variety of electrical discharge sources. Traditional methods of atom detection have included chemical titration,⁴¹ electron spin resonance,^{28,42-44} Wrede-Harteck gauges,¹⁶⁻¹⁸ isothermal calorimeters,^{39,40} and thermocouple probes.^{13,19,20,22-24,45} Some of this early work was summarized in reviews by Kaufman,⁴¹ Brennan,⁴⁶ and Wise and Wood.³⁶

In more recent times, a significant amount of surface catalytic efficiency data have been generated in the MESOX test facility in the PROMES-CNRS laboratory on a variety of ceramic materials.⁴⁷⁻⁵⁰ The MESOX facility uses a flow tube configuration with the test sample facing the oncoming flow. A microwave discharge is used to dissociate air and a unique solar radiation concentrator is used to heat specimens to temperatures as high as 2300 K. O-atom concentration gradients in the vicinity of the sample are inferred using actinometry, a technique based on measuring the relative emission intensities of electronically-excited oxygen and argon atoms at selected wavelengths.^{48,51,52} O-atom recombination coefficients are extracted using an analytic expression for the O-atom gradient approaching the catalytic surface.⁴⁷ Simultaneous measurements of sample temperature enable the estimation of the energy transfer efficiency using an energy balance calculation.⁴⁷

Amouroux and coworkers⁵³⁻⁵⁵ used a similar flow tube configuration to expose a wide range of metallic, oxide and ceramic materials to O-atoms. A radio frequency^{53,54} or microwave discharge⁵⁵ was used to dissociate oxygen molecules and a cartridge heater was used to heat samples to different test temperatures. Recombination coefficients were obtained by fitting an analytic expression for the O-atom gradients near the surface to actinometry data,^{53,54} or calculated from titration data with or without the sample in place.⁵⁵ A flow tube configuration was also used by Mozetič, and coworkers⁵⁶⁻⁵⁸ to study oxygen and hydrogen recombination on steel and niobium surfaces. O-atoms were generated using a radio frequency discharge and recombination coefficients were calculated from measured sample heating curves.

During the 1990's, NASA Ames Research Center supported laboratory measurements of atom recombination coefficients using the diffusion-tube side arm technique, including the study of Kim and Boudart on O, N, and H atom recombination on silica.⁴⁵ In this study, a microwave discharge source was used to generate atomic species, a thermocouple probe was used to measure atomic concentration gradients along the side-arm axis, and a furnace was used to control tube temperatures.

In subsequent work, Pallix and Copeland⁵⁹ introduced the use of laser-induced fluorescence (LIF) as an atom detection method for diffusion tube side-arm reactor experiments. The LIF technique is species specific and minimally intrusive. This avoids many problems associated with the traditional atom detection techniques listed above; e.g., the introduction of contaminants, the disturbance of the gas flow or concentration gradient, the lack of spatial sensitivity, or the lack of species discrimination.

Since 1995, the diffusion tube side-arm reactor in conjunction with laser induced species detection diagnostics has served as the main method by which NASA Ames Research Center has measured O and N atom recombination coefficients in the room temperature to 1000 K range.

4.0 DIFFUSION-TUBE SIDE-ARM REACTOR

4.1 Measurement Theory

The diffusion tube side-arm reactor consists of a dead-end side-arm tube connected at right angles to a main flow tube; see Fig. 1. Free-radical species are produced in the main flow tube upstream of the tube intersection, typically by dissociating molecular gasses using some type of low-pressure electrical discharge. The dissociated species flow past the opening of the side-arm tube. As reactants diffuse into the side-arm tube, they are progressively removed from the gas phase by surface reactions on the walls, establishing a unique steady-state species concentration profile down the length of the tube. This reactor design simplifies subsequent data analysis because gas transport in the side-arm is restricted to species diffusion.

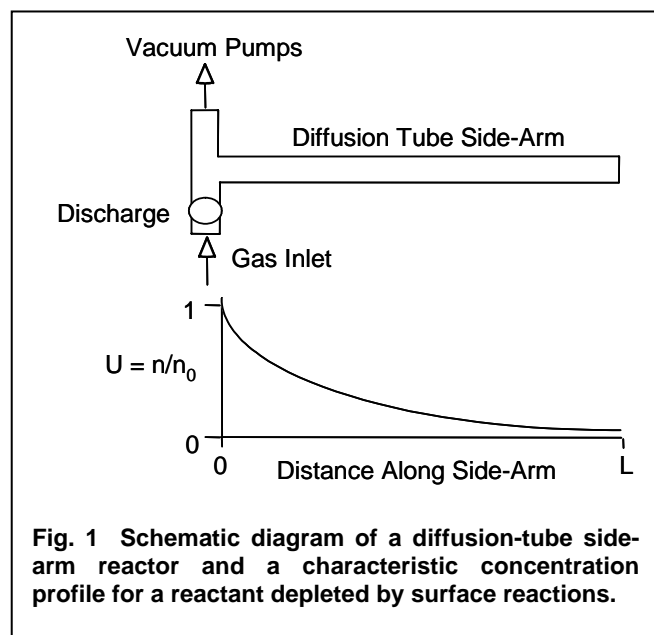


Fig. 1 Schematic diagram of a diffusion-tube side-arm reactor and a characteristic concentration profile for a reactant depleted by surface reactions.

4.2 Diffusion-Reaction Models

The complexity of the diffusion-reaction model required to predict species concentrations in the side-arm reactor depends on many things: the number of gas species present, the number of potential surface reactions and their reaction orders, the number of potential gas-phase reactions, and spatial variations in tube material, geometry, and temperature.

The simplest systems are binary atom-molecule mixtures in a uniform-diameter isothermal tube of a single wall material. Operation at sufficiently low pressures ensures that gas-phase reactions are negligible in comparison to heterogeneous atom losses at the wall, and working with low atom

concentrations ensures that the linear diffusion equation is sufficiently accurate. Further simplifying assumptions are first-order irreversible surface reaction kinetics, a purely catalytic wall, and a single heterogeneous loss pathway leading to atom recombination. Described below are one and two dimensional reaction-diffusion models that can be applied to evaluate surface recombination in binary systems such as O-O₂ and N-N₂.

4.2.1 One-Dimensional Model: Single Wall Material

The most basic solution for the steady-state atom concentration along a finite tube of length L_z is obtained by solving the linear one dimensional diffusion equation with surface loss included as a first-order sink term:

$$D \frac{\partial^2 n}{\partial z^2} - \dot{R}_{\text{sink}} = 0 \quad (23)$$

where $\dot{R}_{\text{sink}} \equiv (\text{loss probability})(\text{atom-surface impingement rate})(\text{surface area per volume})$, or

$$\dot{R}_{\text{sink}} = \gamma_{\text{wall}} \left(\frac{\bar{v}n}{4} \right) \left(\frac{2\pi R dz}{\pi R^2 dz} \right) = \left(\frac{\gamma \bar{v}}{2R} \right) n \quad (24)$$

Here n is the atom number density, z is the axial tube coordinate, R is the tube radius, D is the binary diffusion coefficient, and \bar{v} is the average thermal speed of the atoms. For a binary atom-molecule mixture where the net loss process is heterogeneous atom recombination, the loss probability γ_{wall} is commonly referred to as the recombination coefficient. Appropriate boundary conditions are constant atom concentration at the tube entrance and heterogeneous atom recombination at the tube endplate with loss probability γ_{end} which may differ from that of the tube wall:

$$n(0) = n_0 \quad -D \left. \frac{\partial n}{\partial z} \right|_{L_z} = \gamma_{\text{end}} \frac{\bar{v}n(L_z)}{4} \quad (25a,b)$$

It is useful to recast the equations in non-dimensional form by normalizing the axial coordinate and tube length by the tube radius and the atom concentration by the concentration at the tube entrance; viz., $x \equiv z/R$, $L \equiv L_z/R$ and $U(x) \equiv n(x)/n_0$. This leads to the equation set

$$\frac{\partial^2 U}{\partial x^2} - \lambda^2 U = 0 \quad (26)$$

$$U(0) = 1 \quad \left. \frac{\partial U}{\partial x} \right|_L = -\alpha U(L) \quad (27a,b)$$

$$\lambda = \sqrt{\bar{v}R\gamma_{\text{wall}}/2D} \quad \alpha = \bar{v}R\gamma_{\text{end}}/4D \quad (28a,b)$$

A general solution to Eq. 26 is

$$U(x) = A \cosh(\lambda x) + B \sinh(\lambda x) \quad (29)$$

Evaluation of the constants A and B with the boundary conditions 27a and b gives the particular solution

$$U(x) = \cosh(\lambda x) - \sinh(\lambda x) \left[\frac{\alpha \cosh(\lambda L) + \lambda \sinh(\lambda L)}{\lambda \cosh(\lambda L) + \alpha \sinh(\lambda L)} \right]. \quad (30)$$

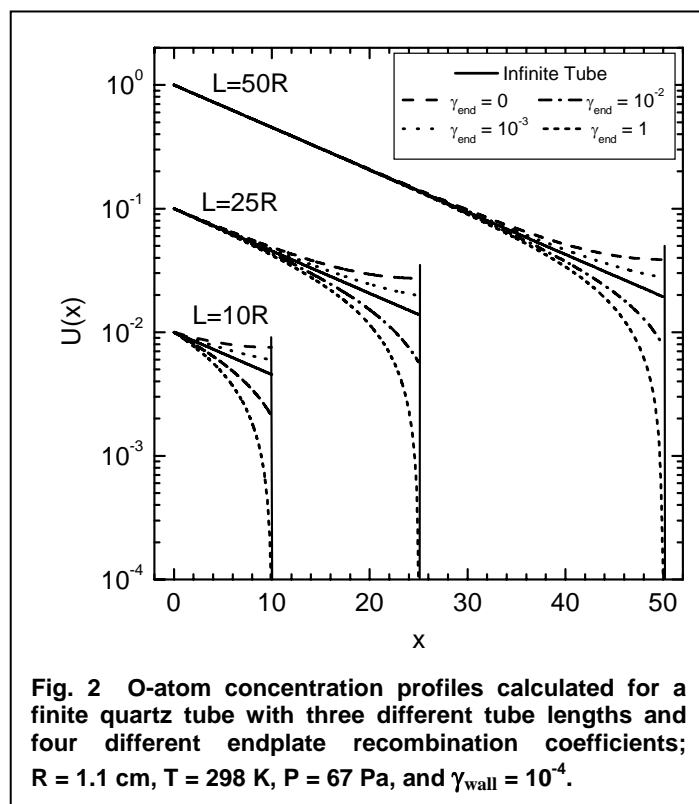
In the limit of an infinitely long tube, the final bracketed term goes to unity and Eq. 30 reduces to the decaying exponential solution

$$U(x) = \exp(-\lambda x). \quad (31)$$

Solutions to Eq. 30, representative of O-atom diffusion into quartz tube at room temperature and low pressure (298 K, 67 Pa, $R = 1.1$ cm, $\gamma_{\text{wall}} = 10^{-4}$) are plotted in Fig. 2 for three different tube lengths and four different endplate reaction efficiencies. The infinite tube solution of Eq. 31 is also included.

Figure 2 illustrates several general features of this diffusion-reaction system. At locations far from the endplate, the atom concentration profile along the tube is well approximated as an exponential decay. In this region, a plot of $\ln(U(x))$ vs x is linear with a slope of $-\lambda$ that can be directly related to the wall catalytic efficiency through Eq. (28a).

As the endplate is approached, the atom concentration profile deviates from a pure exponential dependence on x and this deviation can be either positive or negative depending on the catalytic efficiency of the endplate material. In this region of the tube, the atom concentration profile depends on both γ_{wall} and γ_{end} .



One attractive feature of this binary diffusion-reaction system is that only *relative* values of atom concentrations along the tube are required to relate concentration profiles to the catalytic efficiencies of the wall and endplate materials. Experimentally, relative atom concentrations are much easier to quantify than absolute atom concentrations.

Because the solution for $U(x)$ can be anchored (started) anywhere along the tube, modelling the entire length of the diffusion tube is often unnecessary. For example, if measurements of relative atom concentrations are made over a central region of the tube far from either the opening or the endplate, then the exponential solution (Eq. 31), with $x = 0$ at the location of the first concentration measurement (nearest the tube opening), is sufficient to relate measured concentration profiles to the wall catalytic efficiency.

4.2.2 One-Dimensional Model: Three Tube Sections

Several solutions of the form of Eq. 29 can be joined to model a diffusion tube of multiple sections having walls of different reaction efficiency. A three-section solution is particularly useful for simulating atom concentration profiles along a relatively inert tube containing a more catalytic specimen of finite length. The atom concentration in each tube section of length L_i can be written as:

$$\begin{aligned} U_1(x) &= A_1 \cosh(\lambda_1 x) + B_1 \sinh(\lambda_1 x) \\ U_2(x) &= A_2 \cosh(\lambda_2(x - L_1)) + B_2 \sinh(\lambda_2(x - L_1)) \\ U_3(x) &= A_3 \cosh(\lambda_3(x - L_1 - L_2)) + B_3 \sinh(\lambda_3(x - L_1 - L_2)) \end{aligned} \quad (32a,b,c)$$

To join the different solutions, additional boundary conditions are specified enforcing continuity of atom concentration and concentration gradient at the interfaces between different tube sections. The required constants A_i and B_i are obtained by solving the linear equation set

$$\begin{bmatrix} 1 & 0 & 0 & 0 & 0 & 0 \\ \cosh(\lambda_1 L_1) & \sinh(\lambda_1 L_1) & -1 & 0 & 0 & 0 \\ \lambda_1 \sinh(\lambda_1 L_1) & \lambda_1 \cosh(\lambda_1 L_1) & -\lambda_2 & 0 & 0 & 0 \\ 0 & 0 & \cosh(\lambda_2 L_2) & \sinh(\lambda_2 L_2) & -1 & 0 \\ 0 & 0 & \lambda_2 \sinh(\lambda_2 L_2) & \lambda_2 \cosh(\lambda_2 L_2) & -\lambda_3 & 0 \\ 0 & 0 & 0 & 0 & \lambda_3 \sinh(\lambda_3 L_3) + \alpha \cosh(\lambda_3 L_3) & \lambda_3 \cosh(\lambda_3 L_3) + \alpha \sinh(\lambda_3 L_3) \end{bmatrix} \begin{bmatrix} A_1 \\ B_1 \\ A_2 \\ B_2 \\ A_3 \\ B_3 \end{bmatrix} = \begin{bmatrix} 1 \\ 0 \\ 0 \\ 0 \\ 0 \\ 0 \end{bmatrix} \quad (33)$$

If the tube is infinite, the general solution for the final (third) tube section is replaced by $U_3(x) = A_3 \exp(-\lambda_3(x - L_1 - L_2))$ and equation set 33 is reduced by one order to

$$\begin{bmatrix} 1 & 0 & 0 & 0 & 0 \\ \cosh(\lambda_1 L_1) & \sinh(\lambda_1 L_1) & -1 & 0 & 0 \\ \lambda_1 \sinh(\lambda_1 L_1) & \lambda_1 \cosh(\lambda_1 L_1) & -\lambda_2 & 0 & 0 \\ 0 & 0 & \cosh(\lambda_2 L_2) & \sinh(\lambda_2 L_2) & -1 \\ 0 & 0 & \lambda_2 \sinh(\lambda_2 L_2) & \lambda_2 \cosh(\lambda_2 L_2) & \lambda_3 \end{bmatrix} \begin{bmatrix} A_1 \\ B_1 \\ A_2 \\ B_2 \\ A_3 \end{bmatrix} = \begin{bmatrix} 1 \\ 0 \\ 0 \\ 0 \\ 0 \end{bmatrix} \quad (34)$$

Figure 3 shows the O-atom concentration profiles calculated for a quartz tube $\gamma_1 = \gamma_3 = \gamma_{\text{wall}} = 10^{-4}$ containing samples of three different catalytic efficiencies $\gamma_2 = \gamma_s = 10^{-3}, 10^{-2}, 10^{-1}$. Again, with sufficient separation between the sample location and the end of the diffusion tube, the influence of the endplate catalytic efficiency on the atom concentration profile near the catalytic sample is negligible.

The presence of the catalytic sample distorts the exponential atom concentration profile along the quartz tube. The decay of the atom concentration with distance is accelerated in the region preceding the sample, is most rapid within the sample region, and then recovers the characteristic exponential decay along the quartz tube beyond the sample, though at lower atom concentrations. The larger the difference between the quartz and the sample catalytic efficiencies, the more pronounced these effects. Analogous trends are observed when the

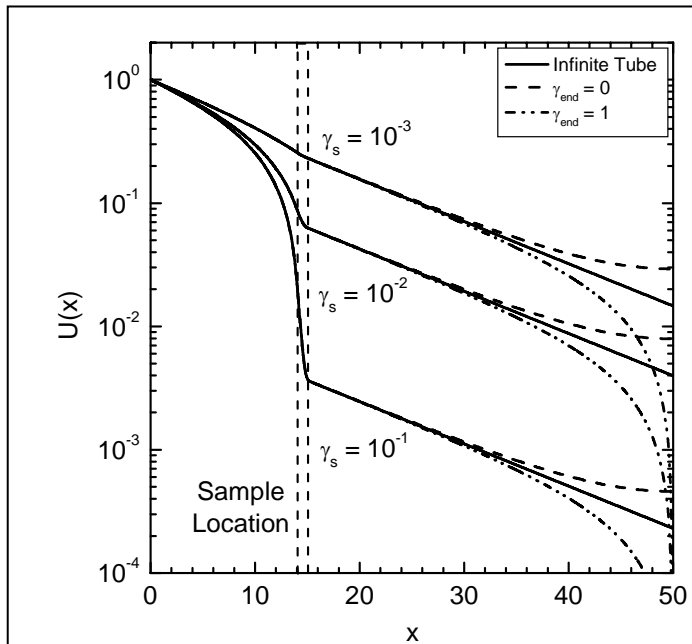


Fig. 3 O-atom concentration profiles calculated for a three-section tube with three different sample and two different endplate recombination coefficients; $R = 1.1$ cm, $T = 298$ K, $P = 67$ Pa, and $\gamma_{\text{wall}} = 10^{-4}$. The lengths of the tube sections are $L_1 = 14R$, $L_2 = 1R$, and $L_3 = 35R$.

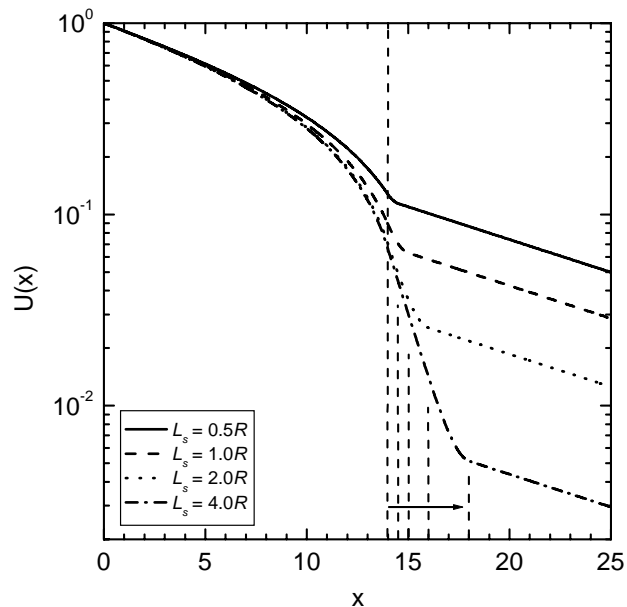


Fig. 4 O-atom concentration profiles calculated for an infinite three-section tube with samples of four different lengths. Same conditions as in Fig. 3; $\gamma_s = 10^{-2}$.

length of a catalytic sample is increased, as shown in Fig. 4.

In an experiment, one would try to measure changes in atom concentration before and after a target sample, and relate these measurements to the catalytic efficiencies of the wall and sample. From an experimental perspective, it is advantageous if concentration profile with the sample in place shows a large deviation from the baseline exponential decay observed for the uniform quartz tube. However, if the sample removes too many atoms from the gas phase, the atom concentration beyond the sample may be too small to detect accurately. The optimal length for a particular test specimen is determined by balancing these two factors, though this can only be estimated before the experiment since the exact catalytic efficiency of the sample is presumably unknown.

3.2.3 Two-Dimensional Model: Arbitrary Tube Sections

The next step in modelling complexity is a two-dimensional diffusion-reaction model that can capture radial concentration gradients. Radial concentration gradients may be important when surface catalytic efficiencies are high. Two-dimensional effects may also become significant near material discontinuities along the wall or near the tube endplate.

For materials with high catalytic efficiencies ($\gamma \rightarrow 1$), the atom velocity distribution function in the vicinity of the surface may become significantly non-Maxwellian, affecting the atom impingement flux. Motz and Wise²⁷ have derived a more accurate expression for the boundary condition at a catalytic surface in a binary mixture with low atom concentrations:

$$-D \frac{\partial n}{\partial x} \bigg|_{\text{wall}} = \frac{\gamma}{(1-\gamma/2)} \frac{n_{\text{wall}} \bar{v}}{4} \quad (35)$$

Note that the $1/(1-\gamma/2)$ correction term only changes the flux by more than 10% for catalytic efficiencies greater than about 0.1.

As long as the atom concentration remains moderate – ratios of atom to molecule concentrations below $\sim 1/5$ – the linear diffusion equation remains satisfactory; in tube-radius normalized cylindrical coordinates

$$\frac{\partial^2 U}{\partial r^2} + \frac{1}{r} \frac{\partial U}{\partial r} + \frac{\partial^2 U}{\partial x^2} = 0 \quad . \quad (36)$$

Wise and co-workers have presented a number of analytic solutions to this equation for different tube and endplate configurations.^{25,27,31,36} Their approach has been extended to include both finite and infinite tubes with N tube sections.⁶⁰ The methodology is summarized below.

Using separation of variables, the solution satisfying Eq. 36 for each tube section has the form

$$U_n(r, x) = F_n(r)G_n(x) = [c_1 J_0(kr) + c_2 Y_0(kr)] [c_3 \cosh(kx_n) + c_4 \sinh(kx_n)] \quad , \quad (37)$$

where $x_n = x - L_{n-1}$ and $L_0 = 0$. The radial boundary conditions for each tube section are i) a symmetric concentration profile about the centreline (zero concentration gradient) and ii) first order atom loss to the tube walls.

$$\left. \frac{\partial U_n}{\partial r} \right|_{0, x_n} = 0 \quad \quad \left. \frac{\partial U_n}{\partial r} \right|_{1, x_n} = -\frac{U(1, x_n)}{\delta_n} \quad (38a,b)$$

with $\delta_n = 4D(1-\gamma_n/2)/\gamma_n \bar{v}R$.

Application of these boundary conditions leads to

$$U_n(r, x_n) = \sum_{i=1}^{\infty} [A_{n,i} \cosh(k_{n,i} x_n) + B_{n,i} \sinh(k_{n,i} x_n)] J_0(k_{n,i} r) \quad , \quad (39)$$

where the $k_{n,i}$ are the positive roots of $J_0(k_{n,i}) = \delta_n k_{n,i} J_1(k_{n,i})$.

To solve for the remaining constants, two axial boundary conditions are required for each tube section. For the first tube section, uniform concentration at the entrance gives

$$U_1(r, 0) = 1 \quad . \quad (40)$$

For the final tube section, two choices are available for finite and infinite tubes, respectively:

$$U_N(r, \infty) = 0 \quad \quad \left. \frac{\partial U_N}{\partial x} \right|_{r, \Delta L_N} = -\frac{U(r, \Delta L_N)}{\delta_{\text{end}}} \quad (41a,b)$$

Additional continuity boundary conditions are imposed at the interfaces between neighbouring tube sections:

$$U_n(r, \Delta L_n) = U_{n+1}(r, 0) \quad \frac{\partial U_n}{\partial x} \bigg|_{r, \Delta L_n} = \frac{\partial U_{n+1}}{\partial x} \bigg|_{r, 0} \quad (42a,b)$$

Application of these boundary conditions results in the following relations:

$$A_{1,i} = \frac{2}{[1 + \delta_1^2 k_{1,i}^2] k_{1,i} J_1(k_{1,i})}, \quad (43)$$

$$B_{N,i} = -A_{N,i}, \quad \text{or} \quad B_{N,i} = -\frac{\delta' k_{N,i} \sinh(k_{N,i} \Delta L_N) + \cosh(k_{N,i} \Delta L_N)}{\delta' k_{N,i} \cosh(k_{N,i} \Delta L_N) + \sinh(k_{N,i} \Delta L_N)} A_{N,i}. \quad (44a,b)$$

$$A_{n,i} = \cosh(k_{n,i} \Delta L_n) \sum_{j=1}^{\infty} R_n(i, j) A_{n+1,j} - \frac{\sinh(k_{n,i} \Delta L_n)}{k_{n,i}} \sum_{j=1}^{\infty} k_{n+1,j} R_n(i, j) B_{n+1,j} \quad (45)$$

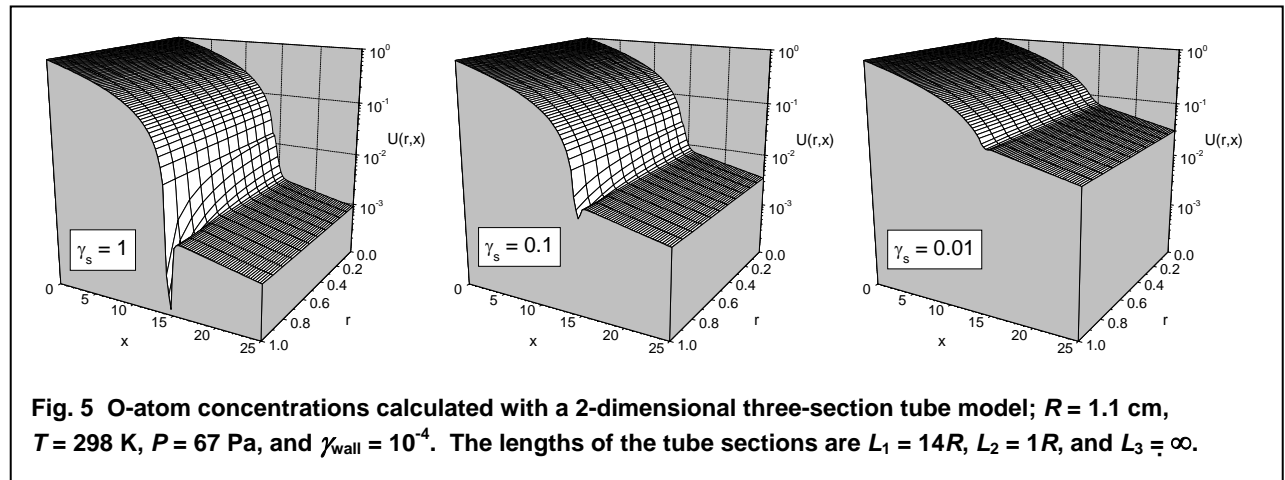
$$B_{n,i} = -\sinh(k_{n,i} \Delta L_n) \sum_{j=1}^{\infty} R_n(i, j) A_{n+1,j} + \frac{\cosh(k_{n,i} \Delta L_n)}{k_{n,i}} \sum_{j=1}^{\infty} k_{n+1,j} R_n(i, j) B_{n+1,j} \quad (46)$$

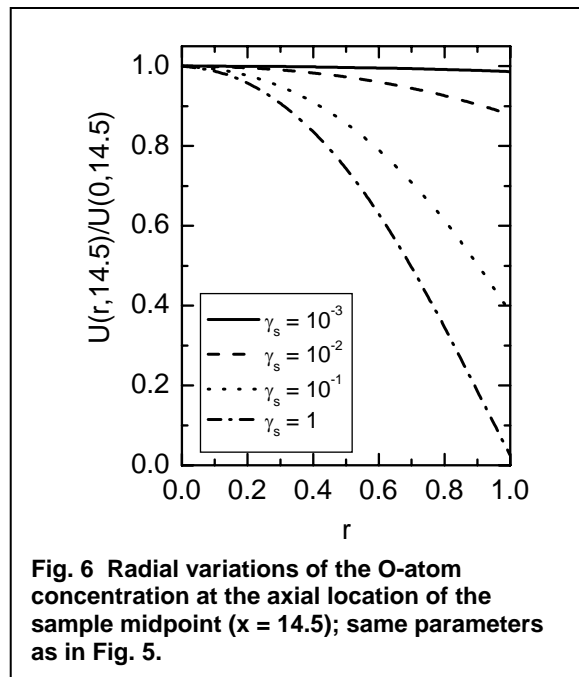
with

$$R_n(i, j) = \frac{2k_{n,i} k_{n+1,j} [\delta_n - \delta_{n+1}] J_1(k_{n+1,j})}{[k_{n+1,j}^2 - k_{n,i}^2] [1 + \delta_n^2 k_{n,i}^2] J_1(k_{n,i})} \quad (47)$$

These relations can be represented as a set of matrix equations that can be evaluated numerically to a specified accuracy (i.e., to the I^{th} approximation of the infinite series).⁶⁰

Figure 5 shows examples of the 2-dimensional O-atom concentration profile computed for a room-temperature quartz tube containing a catalytic sample of $\gamma_s = 1, 0.1$, or 0.01 . The concentration along the centreline ($r = 0$) varies smoothly with axial location, even in the vicinity of the highly catalytic sample. Strong radial gradients are observed in close proximity to the highly catalytic wall.





The radial variation in atom concentration at the sample midpoint location ($x = 14.5$) is plotted in Fig. 6. Note that the atom concentration near the centreline does not change rapidly in the radial direction, even for the fully catalytic sample. The radial distortion of the atom concentration is rapidly dissipated before and after the sample along the axial direction.

4.3 Species Detection

In LIF detection, a tunable laser is used to generate light at a wavelength resonant with a particular electronic transition in the atom or molecule of interest. Absorption of this light excites the target species to a higher-energy electronic state. The excited species subsequently emits photons as it drops back down to a lower energy state. The intensity of this fluorescence is directly proportional to the initial number of ground state species in the gas volume excited by the laser, provided that competitive losses from the upper state, such as ionization, amplified

spontaneous emission, and collisional quenching, are minimized.

For the detection of ground-state atomic oxygen and atomic nitrogen, Pallix and Copeland⁵⁹ applied two-photon LIF schemes that were originally developed at SRI International^{61,62} and have seen wide application in combustion diagnostics. More recently, an alternate two-photon scheme for N-atoms has been used.⁶³ The relevant energy level diagrams for oxygen and nitrogen are shown in Figs. 7 a,b,c.⁶⁴

The oxygen atom ground state has three fine structure components (for $J = 2, 1$, or 0) that are populated at thermal equilibrium according to the Boltzmann distribution. The $J = 2$ component has the highest relative population over the temperature range of the experiment, ranging from about 74% at 300 K to 60% at 1500 K. Ultraviolet radiation near 226 nm is used to excite the $J = 2$ component of ground state oxygen via the $3p^3P_{1,2,0} \leftarrow 2p^3P_2$ two-photon transition. The excited state has a radiative lifetime of 33.3 ± 1.7 ns and an O_2 quenching constant of $(7.8 \pm 0.8) \times 10^{-10} \text{ cm}^3 \text{ s}^{-1}$.⁶⁵ Fluorescence occurs via the $3p^3P_{1,2,0} \rightarrow 3s^3S_1^0$ transitions. The three fine structure components of the $3p^3P$ state are within 1 cm^{-1} of each other. Thus, the fluorescence wavelength is about 845 nm for radiative transitions originating from any of the three upper states.

Ground-state nitrogen atoms can be detected using two different two-photon schemes. The energy level diagram for the traditional scheme is shown in Fig. 7b.⁶⁴ The $3p^4D_{7/2}^0 \leftarrow 2p^3^4S_{3/2}^0$ two-photon transition is excited using ultraviolet radiation at 211 nm. The radiative lifetime of the upper state is about 43 ± 3 ns and the N_2 quenching constant is $(4.6 \pm 0.6) \times 10^{-10} \text{ cm}^3 \text{ s}^{-1}$.⁶⁶ Fluorescence near 868 nm is obtained from the $3p^4D_{7/2}^0 \rightarrow 3s^4P_{5/2}$ radiative transition. The $3p^4D^0$ state has four fine structure components ($J = 1/2, 3/2, 5/2$, and $7/2$) and the $3s^4P$ state has three fine structure components ($J = 1/2, 3/2$, and $5/2$). Therefore, a manifold of allowed transitions ($\Delta J = 0, \pm 1$) exist between these two states. The advantage of preparing the $3p^4D_{7/2}^0$ state is that the entire fluorescence signal is concentrated at one wavelength because only the $\Delta J = -1$

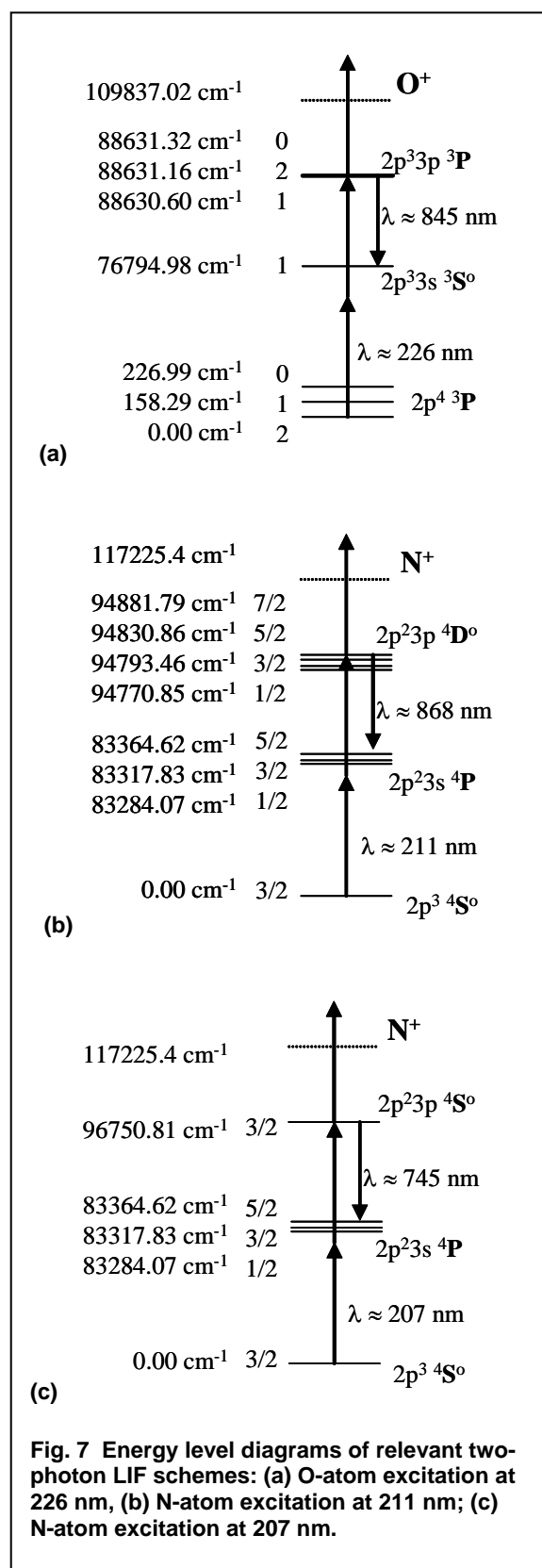


Fig. 7 Energy level diagrams of relevant two-photon LIF schemes: (a) O-atom excitation at 226 nm, (b) N-atom excitation at 211 nm; (c) N-atom excitation at 207 nm.

transition is allowed. Collisional transfers among the multiplets of the excited nitrogen state are possible,⁶⁷ however at pressures below ~0.5 Torr (67 Pa) this transfer is probably not significant. Additionally, the most probable intramultiplet transfer is from the 7/2 to the 5/2 state, which fluoresces predominantly near 868 nm and still contributes to the measured signal.

The energy level diagram for a second two-photon LIF scheme for N-atom detection is given in Fig. 7c.⁶⁴ The $3p^3 4S^0_{3/2} \leftarrow 3p^3 4S^0_{3/2}$ two-photon transition is excited by ultraviolet radiation near 207 nm. The radiative lifetime of the $3p^3 4S^0_{3/2}$ upper state is about $26 \pm 2 \text{ ns}$ with an N_2 quenching rate constant of $(6.7 \pm 0.9) \times 10^{-11} \text{ cm}^3 \text{ s}^{-1}$.⁶³ Fluorescence occurs near 745 nm via the $3p^3 4S^0_{3/2} \rightarrow 3s^2 4P^0_{5/2,3/2,1/2}$ radiative transitions. This scheme has the advantages that the collisional quenching rate constant is significantly smaller and that the fluorescence is at shorter wavelengths than the traditional scheme.

4.4 System Configuration

Figure 8 shows a diagram of the diffusion tube side-arm reactor facility at NASA Ames Research Center. Similar facilities have been set up at SRI International.

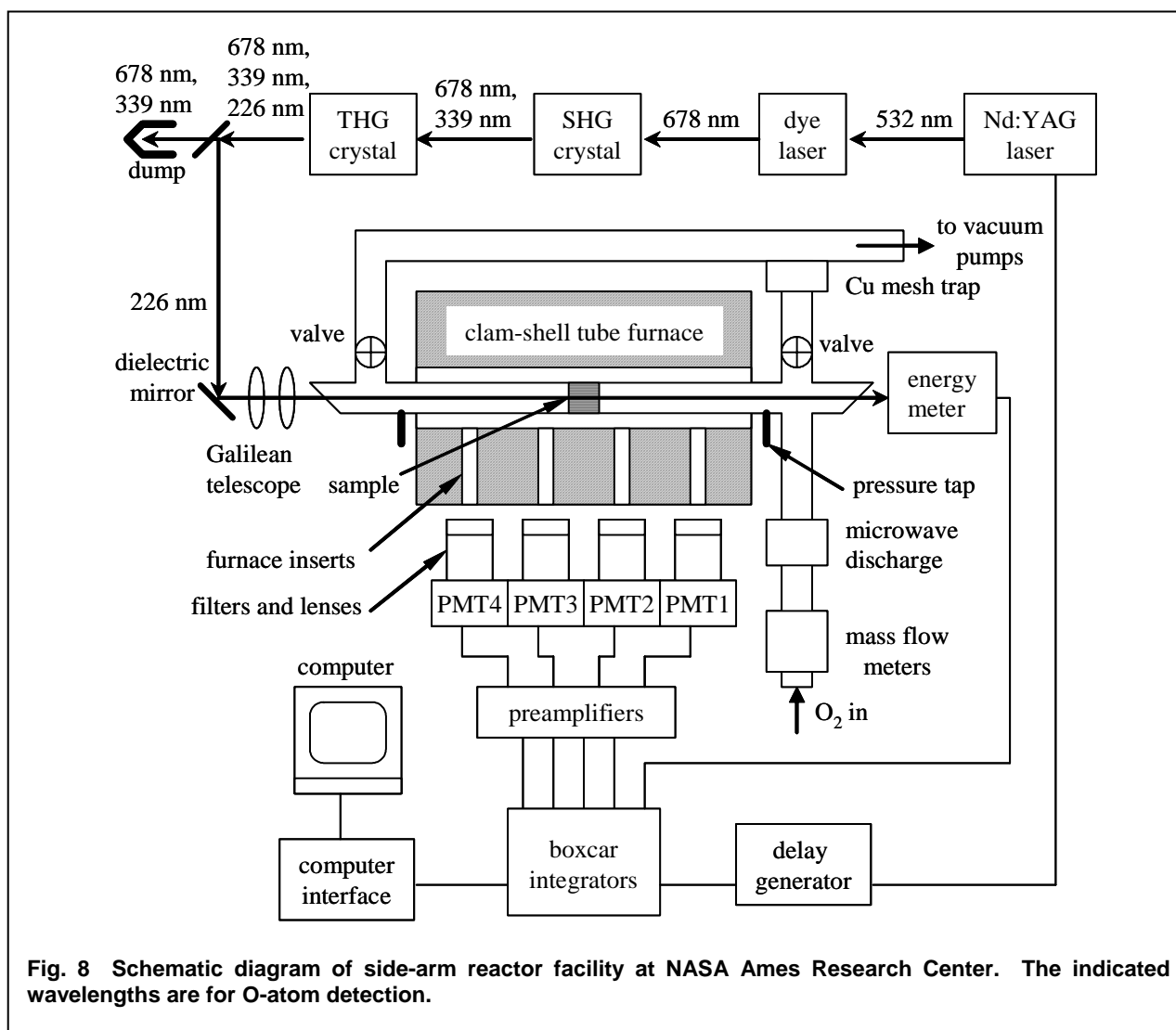
The reactor consists of a glass main arm and a quartz side arm joined at a quartz cross. Approximately 47 cm (18 inches) of the side arm tube is enclosed in a three-section Lindberg electric clam-shell furnace capable of reaching ~1500 K. Test samples in the form of tubes are placed inside the side-arm tube near the center of the furnace.

Gases are introduced into the main arm upstream of the cross. By a simple adjustment of valves (see Fig. 8) the side arm can be turned into either a dead-end diffusion tube or a flow tube. In both cases gases are evacuated by a Varian V-90 turbomolecular pump backed with a mechanical pump. A fluorinated pump oil (Fomblin) is used in the mechanical pump to avoid explosion hazards when pumping oxygen.

Gas flow is measured using calibrated Tylan flow meters and gas pressures are measured using a 1 Torr Baratron capacitance manometer gauge. High purity oxygen and nitrogen gases (99.998%) are used directly from their

cylinders. Typical gas flow rates are 10-20 standard cubic centimeters per minute (sccm) and typical reactor pressures are ~40 Pa (0.3 Torr). A microwave discharge is positioned on the main arm upstream of the cross. The discharge operates at 2450 MHz and is powered by an Ophos power supply. Molecular oxygen or nitrogen is introduced into the reactor upstream of the discharge. The discharge is lit using a Tesla coil. During operation, the discharge is operated at powers between 40 W and 100 W, with 90 W being typical, and is convectively cooled using compressed air. Chemical titration experiments indicate that oxygen dissociation fractions are in the 1-3% range, with nitrogen dissociation about one order of magnitude lower.

The $O + O_2 + Z \rightarrow O_3 + Z$ gas phase three-body reaction becomes significant at pressures above about 65 Pa (0.5 Torr). To eliminate the influence of this gas phase reaction on species concentration profiles, the total reactor pressure is always kept below 53 Pa (0.4 Torr). The $O + O + Z \rightarrow O_2 + Z$ reaction, although ~5 times faster than the ozone producing reaction at room temperature, is less important because of the low O-atom concentrations present in the system.



Tunable red light is provided by a Continuum ND60 dye laser pumped by the second (532 nm) harmonic of a Continuum NY81 Nd:YAG laser. For O-atom detection, red light is generated near 678 nm using LDS 698 laser dye. For N-atom detection red light is generated near 621 nm using Rhodamine 640 laser dye, or near 633 nm using DCM laser dye. All three dyes are dissolved in HPLC grade methanol. Ultraviolet radiation for atom excitation is obtained by frequency tripling the red light using two beta-barium borate (BBO) crystals for second and third harmonic generation. The same BBO crystals can be used for all three excitation schemes.

Residual red light in the beam is separated from the desired UV radiation using several dichroic mirrors. The beam is directed through a down-collimating Galilean telescope, through a quartz window oriented at Brewster's angle and down the centerline of the side arm tube. The laser pulse energy is monitored with a Molelectron J3-09 pyroelectric energy meter that intercepts the beam as it exits the reactor through a similar Brewster's angle window located on the cross.

Fluorescence is detected at normal incidence by four red-sensitive Hamamatsu R636 photomultiplier tubes (PMTs) with gated C1392 sockets. Gated operation reduces saturation from background light. The PMT anode bias voltages of -1300 V are provided by four high voltage DC power supplies. A single custom built +250 V DC power supply is used to supply the PMT gate voltages. A periodic external trigger signal removes this gate voltage, allowing the PMT anode biases to be applied.

A wedge shaped refractory insert allows optical access while the furnace is closed and operating. This refractory insert has 1 cm diameter optical ports lined with quartz tubes to view the centerline of the side-arm tube every 8.9 cm (3.5 inches) along its axis. The pseudo-collimated light emerging from the ports is collected by the PMTs, which are fitted with narrow-band interference filters (~3 nm bandwidth) centered at 845 for O-atom detection and 745 nm for N-atom detection. The PMTs are labeled 1 through 4 in Fig. 8, with PMT1 the closest to the side-arm opening. Test samples are positioned between the regions viewed by PMT2 and PMT3.

A Stanford Research Systems data acquisition system is used along with a personal computer to collect, process, and store output signals from the energy meter and the four PMTs. The data acquisition system consists of an SR240 preamplifier, five SR250 boxcar integrators, and an SR245 computer interface all housed in an SR280 mainframe. The Nd:YAG laser, the gated PMTs and the data acquisition system are triggered at 10 Hz and timed with respect to one another using a Stanford Research System DG535 digital delay and pulse generator.

4.5 Experimental Procedures

4.5.1 PMT Normalization

The fluorescence detection sensitivity at the four PMTs differs for a number of reasons: PMT sensitivity, filter transmission characteristics, and alignment of the detection optics and laser beam alignment. These differences must be accounted for when using the relative PMT signals at the different positions as proxies for the relative atom concentrations. Relative PMT sensitivities can be trivially determined when detecting stable species, by simply filling the tube with a uniform stagnant gas. However, this is not possible for reactive species such as O or N atoms since they are lost on the walls and hence not uniformly distributed.

An initial approach to this problem was to measure the relative PMT response to the thermal background of the heated furnace; however, this proved unsatisfactory for a number of reasons. One problem is that thermal

gradients exist in the furnace walls since the embedded heating elements are hotter than the surrounding surfaces. It is not assured that all four PMTs view similar backgrounds. Additionally, the LIF signal is collected from a line source (the excited atoms in the laser beam path) while thermal radiation appears as a disk source, consequently focusing differently on the PMT cathodes. Also, the convolution of the filter transmission band with a uniform thermal radiation background does not capture differences in LIF sensitivity due to the wavelength alignment of the filter band pass with the atomic line emissions.

An alternate approach, currently in use, is to use LIF signals collected with the reactor configured as a flow tube as normalizing factors. This approach removes uncertainties introduced by using an emission source of different geometry and wavelength characteristics than the atom fluorescence to be detected. The side-arm can be turned into a flow tube by simple adjustment of two valves, as shown in Fig. 8.

Fast flow minimizes differences in atom concentrations between the different PMT locations because the influence of surface reactions is greatly diminished. However, surface losses cannot be completely eliminated and the pressure gradients that drive the flow also cause axial variations in number density. In order to use LIF measurements made in flow tube mode as normalizing factors for fluorescence detection sensitivity, the collected signals must first be corrected for both wall losses and pressure effects. A correction procedure is described below

The relationship between mass flow \dot{m} and the pressure (P_1, P_2) at two axial locations (x_1, x_2) in a uniform tube of radius R can be described using the Hagen-Poiseuille relation including a correction for slip at the wall:

$$\dot{m} = \left[\frac{\pi R^4 M}{8 \mu R T} \right] \frac{P_1 - P_2}{x_1 - x_2} \left[\frac{P_1 + P_2}{2} + \frac{\mu}{R} \sqrt{\frac{8 \pi R T}{M}} \right] ; \quad (48)$$

R is the universal gas constant, M molar mass, and μ is the viscosity. The sufficiency of this relation in describing the flow can be checked by measuring pressures on either side of the furnace, calculating the mass flow rate, and comparing the value to that measured with the mass flow meter. Generally, discrepancies between calculated and experimental mass flow rates are less than 10%. Combining mass conservation and the perfect gas law allows calculation of the bulk flow velocity at each PMT position:

$$v = \frac{\dot{m} R T}{\pi R^2 P M} . \quad (49)$$

The ratio of the actual atom number densities viewed by two PMTs at different axial locations can be approximated by a simple one-dimensional flow analysis leading to

$$\frac{n(x_2)}{n(x_1)} = \frac{P_2}{P_1} \exp \left(- \frac{\gamma \bar{v} (x_2 - x_1)}{R (v_2 + v_1)} \right) , \quad (50)$$

where the wall loss probability must initially be estimated.

The pressure gradient has the additional effect of changing the fluorescence yield and the fraction of fluorescence collected at each position. The ratio of measured fluorescence at two different PMT locations viewing the same atom concentration is approximately

$$\frac{f_2}{f_1} = \frac{\tau_{eff,2}}{\tau_{eff,1}} \frac{1 - \exp\left(-\frac{\tau_g}{\tau_{eff,2}}\right)}{1 - \exp\left(-\frac{\tau_g}{\tau_{eff,1}}\right)}, \quad (51)$$

where τ_g , is the gate length of the boxcar integrator, and the effective lifetime of the excited state is given in terms of the natural radiative lifetime τ_{rad} and the quenching rates $k_{q,i}$ of the collision partners by

$$\frac{1}{\tau_{eff}} = \frac{1}{\tau_{rad}} + \sum_i n_i k_{q,i}. \quad (52)$$

In practice, the fluorescence collection corrections amount to only 1 or 2 %, while the corrections for wall loss and pressure differences can approach 25% between PMT1 and PMT4. Because of their sensitivity to beam and PMT alignment, the fluorescence detection sensitivities are re-measured periodically during every testing program. A consistent value of loss probability can be obtained by iterating between flow tube and diffusion tube measurements several times.

4.5.2 Measurement Sequence

The data collection for a typical test consists of acquiring approximately 200 bins of data on five channels (i.e., the energy meter and four PMTs), with each bin containing the mean signal from 10 laser shots. The appropriate baseline offset is subtracted from each bin, and the average signal and associated standard deviation are calculated for each channel. The average PMT signals and the standard deviations are then corrected for the relative detection sensitivities at the different PMT locations. The final corrected PMT signals are directly proportional to the species concentration at each detection location and are fit by analytic solutions to extract recombination coefficients.

In order to extract recombination coefficients for samples of interest, the atom loss on the quartz reactor walls must either be measured, assumed known, or estimated during the data fitting procedure. Typically, atom recombination coefficients on the quartz side-arm tube are measured as a function of temperature several times before and after testing other materials, to capture any systematic changes that have been caused by temperature cycling or contamination from out-gassing samples.

For the geometry and dimensions of the side-arm reactor facility at NASA Ames Research Center, the simple one-dimensional exponential solution for an infinite tube (Eq. 31) provides a sufficiently accurate description of the atom decay along the tube centreline. Fits of $\ln(U(x))$ vs x to the measured data at the four PMT locations yields a slope that is directly related to the recombination coefficient (via Eq. 28a.)

With quartz recombination coefficients in hand, data measured with a sample inside the side-arm can be fit using solutions to a three section tube model, with the recombination coefficient for the first and third sections fixed at the experimental value. Again, the infinite tube solutions are sufficient for the final side-arm section. In practice, centreline solutions to the 2-dimensional diffusion model are used to match experimental data (Eq. 39), though the 1-dimensional three-section tube model provides similar results.

4.6 Examples of Experimental Results

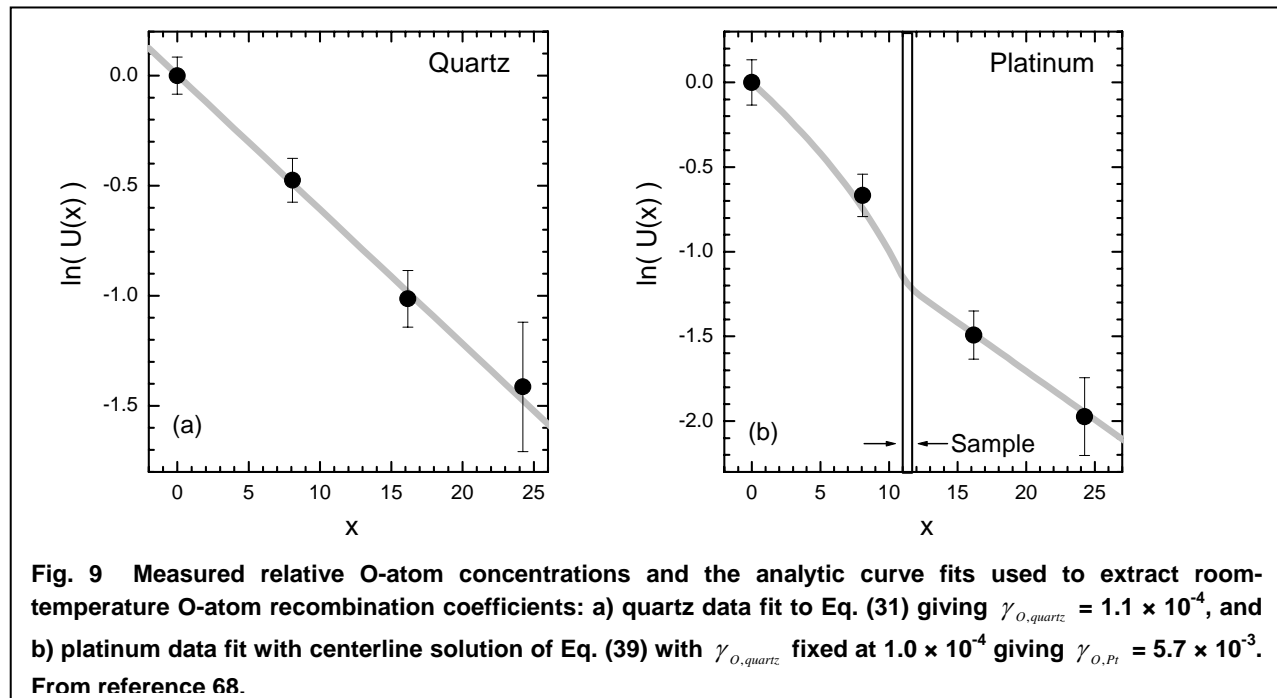
The majority of the side-arm reactor data generated for a variety of TPS materials during the late 1990's is summarized in publicly available NASA reports and AIAA conference papers.^{9-11,60} Additional measurements are contained in proprietary documents.

Figures 9a and b show experimental data and curve fits used to extract O-atom loss probabilities on quartz and platinum surfaces, during a recent side-arm reactor study to support shock tube experiments conducted in dissociated CO₂.⁶⁸ Table 2 lists the number of independent determinations, the average room temperature values, and the standard deviations of the O-atom loss probabilities obtained for quartz, stainless steel 304, Constantan, Chromel, and platinum samples. The standard deviations reflect the reproducibility of the experimental measurements, which were made over the course of several days for each material.

The measured $\sim 1 \times 10^{-4}$ value of O-atom loss probability on room temperature quartz is well within the wide range of experimental values that have been reported in the literature. For example, Berkowitz⁶⁹ cited 15 different determinations that produced values from $(0.17 - 7.1) \times 10^{-4}$ for measurements on silica, quartz, Pyrex and Vycor samples, and Marschall⁶⁰ cited 8 different measurements made on quartz surfaces that span the range $(0.27 - 2.5) \times 10^{-4}$.

Table 2: Room-Temperature O-atom Loss Probabilities

Material	Experiments	$\gamma_{O, \times 10^{-3}}$
Quartz	11	0.098 ± 0.013
SS304 (Cr 18%, Ni 10%, Fe balance)	11	16 ± 7
Constantan (Ni 45%, Cu balance)	10	46 ± 17
Chromel (Cr 10%, Ni Balance)	9	6.8 ± 1.3
Platinum (99.95% Pure)	10	5.3 ± 1.1

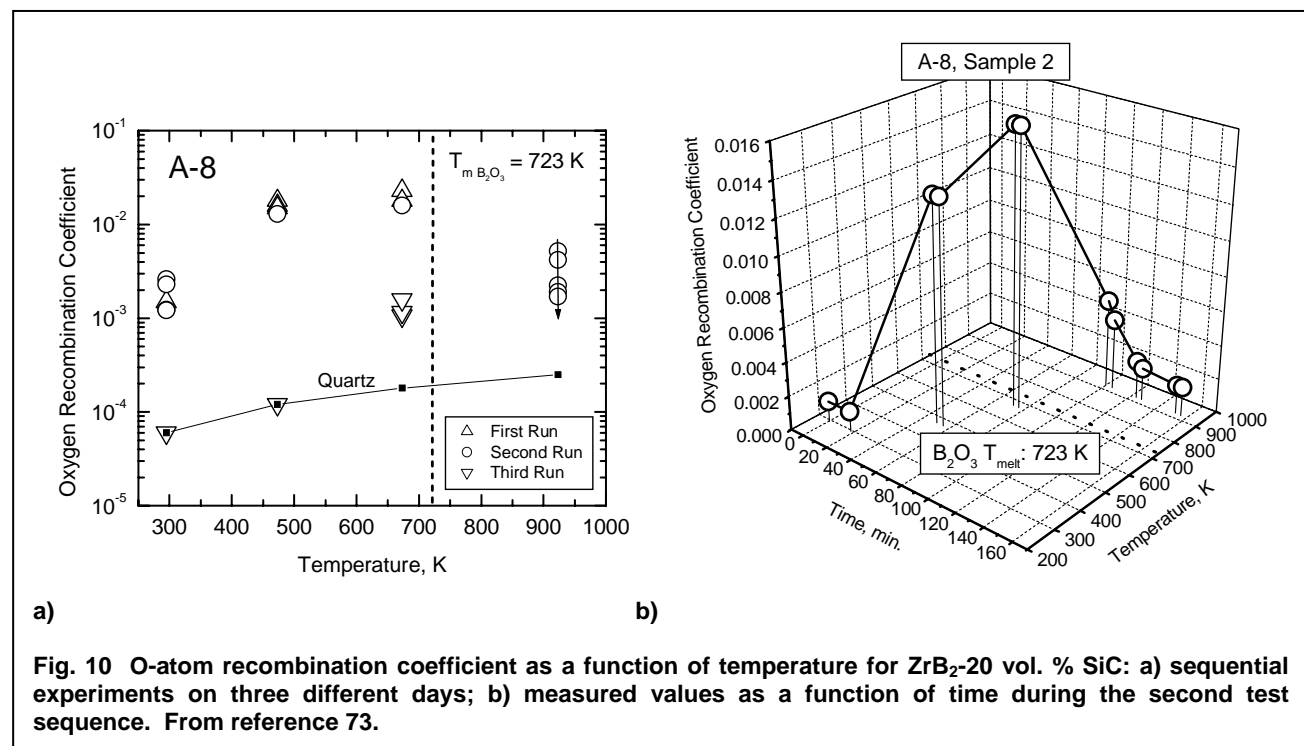


The value of $(16 \pm 7) \times 10^{-3}$ measured for stainless steel 304 can be compared to $(70 \pm 9) \times 10^{-3}$ reported for the same material by Mozetič and Zalar,⁵⁷ $(7.1 \pm 1.4) \times 10^{-3}$ reported for “steel” by Cauquot et al.⁵⁵, and $(10 \pm 4) \times 10^{-3}$ reported for Fe by Melin and Madix.¹⁵ It is highly likely that most metallic surfaces are covered by thin layers of oxide scales. Dickens and Sutcliffe⁷⁰ give a value of 8.5×10^{-3} for Fe_2O_3 and Guyon et al.⁵⁴ give $(15 \pm 3) \times 10^{-3}$ for Fe_3O_4 . The value of $(5.3 \pm 1.1) \times 10^{-3}$ measured for platinum can be compared to $(4 \pm 3) \times 10^{-3}$ given by Hartunian et al.,⁷¹ and $(14 \pm 4) \times 10^{-3}$ reported by Melin and Madix.¹⁵

No O-atom recombination coefficients have been reported for Constantan or Chromel samples. However, for copper and nickel samples, Melin and Madix¹⁵ measured $(15 \pm 5) \times 10^{-3}$ and $(17 \pm 5) \times 10^{-3}$, Myerson⁷² measured 31×10^{-3} and 8.5×10^{-3} , and Hartunian et al.⁷¹ reported $(150 \pm 50) \times 10^{-3}$ and $(40 \pm 20) \times 10^{-3}$. The more recent measurement of Cauquot et al.⁵⁵ for copper is $(25 \pm 5) \times 10^{-3}$. Data cited by Melin and Madix,¹⁵ as well as the measurements of Dickens and Sutcliffe,⁷⁰ suggest that copper oxides are about one order of magnitude more catalytic than nickel oxides. Thus it is perhaps reasonable that the Cu containing Constantan alloy is more catalytic than the Ni-rich Chromel alloy.

A major source of discrepancies among atom recombination coefficients reported in the literature for nominally identical materials can safely be attributed to differences in the surface morphology (e.g., microscopic roughness) and surface composition (e.g., oxidation). In most studies the condition of the surface before and after testing is not characterized.

During recent measurements of surface catalytic efficiency on HfB_2/SiC and ZrB_2/SiC monolithic composites, experimental results clearly indicated that the catalytic properties were changing during testing.⁷³ Each sample was tested on three different days, at several discrete temperatures, with multiple measurements at each temperature. During the first test run measurements were made at 295 K, 473 K, and 673 K, during the second test run these measurements were repeated and extended to 923 K, and during the third test run



measurements at all four temperatures were repeated once more. The reactor was not opened between runs and the samples remained continuously under vacuum.

Figures 10a and b show the results. During the first test, room temperature recombination coefficients were $\sim 1\text{--}2 \times 10^{-3}$. Upon heating to 473 K, the recombination coefficients rise by an order of magnitude to $\sim 1\text{--}2 \times 10^{-2}$. With further heating to 673 K they increase slightly to the $\sim 2\text{--}3 \times 10^{-2}$ range. During the second test sequence, the measured recombination coefficients at each of these three temperatures are basically the same within some experimental scatter. When the sample is heated to 923 K, a steady decrease in catalytic efficiency with time is observed as indicated by the downward arrow in Fig. 10a. The trend is more clearly shown in Fig. 10b, which plots the measured recombination coefficient as a function of time and temperature. During the third test, the sample's catalytic efficiency for O-atom recombination is drastically reduced, by one to two orders of magnitude, to the point that the recombination coefficients of the test specimen cannot be distinguished from those of the quartz tube at the two lowest test temperatures.

This change in catalytic efficiency is an indication that the surface of the test specimen is changing. The most likely process is surface oxidation, an interpretation supported by energy dispersive X-ray analysis (EDX) and X-ray photoelectron spectroscopy (XPS) conducted on identical samples exposed to similar oxidizing environments and heating cycles.⁷³ SiC oxidation under the oxygen and temperature conditions of the side-arm reactor during catalysis testing should be negligible; however, oxidation of the diboride to form zirconia and B_2O_3 is possible and the large drop in surface catalytic efficiency correlates well with the first temperature excursion above the B_2O_3 melting point of ~ 723 K during the second test sequence.

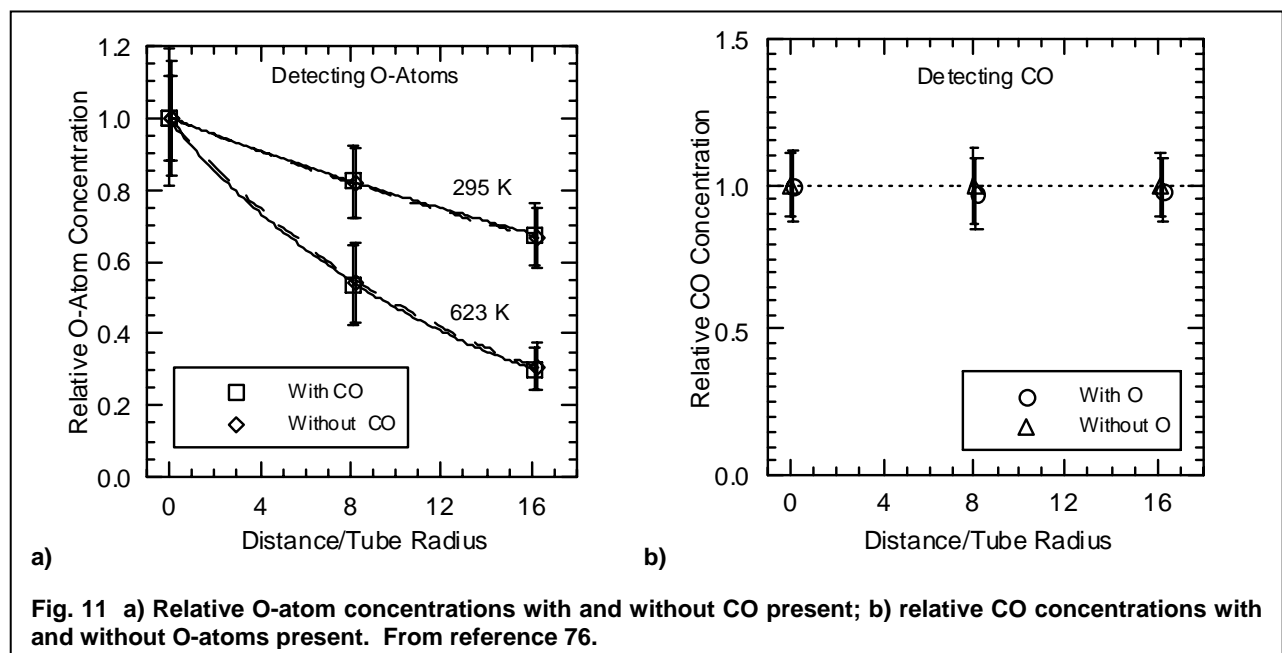
The side-arm reactor has also been used to investigate catalytic phenomena in a qualitative way. In a study by Copeland et al.,⁷⁴ a nitrogen discharge was titrated by adding NO downstream to produce O-atoms by the fast gas phase reaction $\text{N} + \text{NO} \rightarrow \text{N}_2 + \text{O}$ ($k = \sim 3 \times 10^{-11} \text{ cm}^3 \text{ s}^{-1}$). As the NO flow is increased, the concentration of N-atoms falls and the concentration of O-atoms rises. At the titration endpoint all N-atoms produced by the discharge are consumed. Further additions of NO to the reactor result in the appearance of NO in the gas-phase. Laser induced fluorescence was used to simultaneously monitor N-atom and NO concentrations at locations downstream of the titration inlet.

Downstream of the NO inlet only surface reactions can change the concentrations of N and O atoms significantly, because all other gas-phase reactions are too slow under the low pressure conditions of the experiment. In a flow tube environment surface reactions are minimized and the decay of N-atom concentration was observed to be linear with NO addition. However, in a diffusion tube environment, a greater than linear dependence on NO addition was consistently observed during the initial portion of the titration curve, and N-atom losses were greater than expected when O-atoms were present in comparable concentrations. The likely explanation for this observation is that $\text{O} + \text{N}$ recombines to NO on the surface and that the desorbing NO molecule quickly consumes another N atom via the titration reaction. This cycle effectively enhances N-atom loss from the gas-phase. Kurotaki has shown how this mechanism is important for simulating measured heat flux data on the OREX flight experiment using a mechanistic surface chemistry model similar to that in Table 1.⁷⁵

Experiments have also been performed to look for qualitative indications of the relative importance of the $\text{O} + \text{O}$ and $\text{O} + \text{CO}$ surface reactions, as might be important for Mars atmospheric entries.^{68,76} In these studies, LIF was used to look for changes in either the O-atom or CO concentration with the addition of the other species to the reactor. Experiments were performed in $\text{O}_2/\text{O}/\text{CO}/\text{He}$ gas mixtures, on quartz, and a variety of metal samples, including Inconel 617 and all the metals listed in Table 2.

Figure 11 shows the results of these types of experiments on quartz.⁷⁶ No significant or systematic changes are observed in the concentration profiles of either gas species with the introduction of the other. If the $O + CO$ reaction were operating efficiently, one would expect to see the exponential O-atom profile along the side-arm decay more rapidly in the presence of CO and the uniform CO concentration change to a decaying profile in the presence of O-atoms. However neither of these changes is seen in Figs. 11a or b.

Similar measurements with Inconel 617 at room temperature,⁷⁶ and SS304, Constantan, and Chromel at room temperature and 250 °C,⁶⁸ also suggest that the $O + CO$ reaction is not competitive with the $O + CO$ reaction on these materials under the pressure, temperature, and gas composition of these experiments. For platinum at room temperature the same result is found. At 250 °C the well known surface catalyzed $O_2 + 2CO$ oxidation reaction was clearly observed, and no additional effect of O-atoms could be discerned.



4.7 Accuracy, Reproducibility, and System Improvements

The “absolute” accuracy of measured loss coefficients is problematic to define. There are no reference standards that can be used with any confidence. Examples can be found in the literature where certain materials – typically copper or silver surfaces – have been used as reference materials with “known” values for recombination coefficients. However, any cursory survey of the literature quickly uncovers numerous measured values for each material, many of which do not agree within their stated uncertainties. This should not be surprising. First, loss coefficients obtained are “effective values” in the sense that both the intrinsic material chemistry and the microscopic reactive surface area contribute to the measured value. For aerospace applications, this highlights the importance of conducting measurements on test samples that reproduce as closely as possible the material source and fabrication techniques used in the actual TPS components. Second, loss coefficients extracted from the experimental data are closely coupled to the surface chemistry and gas flow assumptions used during data analysis. Because these vary with different techniques, only measurements made using the same experimental and data analysis approaches can really be expected to agree

closely. A broad (and admittedly subjective) review of published measurements suggests that any individual experimental result is probably uncertain by a factor of at least 3 when taken to represent a particular type of material such as “steel” or “silica”.

For a chemically stable low catalytic efficiency material such as quartz, measurements made in rapid succession in the diffusion-tube side-arm reactor generally produce recombination coefficients that differ by less than 10%. Exceptions occur at high temperatures where the decreasing atom number density and the increasing thermal background from the furnace degrades the signal-to-noise ratio, or when initial heating or discharge operation produces transients associated with the removal of surface contaminants such as water. For materials with higher catalytic efficiency the scatter in successive measurements is typically higher at a given temperature because more atoms are removed from the gas phase, lowering the LIF signal. However, this scatter still rarely exceeds 25%. Measurements made on different days, especially after temperature cycling, can yield values that differ by 50% or more, as reflected in the data listed in Table 2 for the metals. These larger changes are typically due to the evolution of the sample in response to the test environment, but may also contain contributions from various subtle changes in the experiment; e.g., optical alignments, excitation beam shape, etc.

Many improvements can be made in both the experimental and data analysis techniques to extend the experimental range of the apparatus and to make the resulting experimental data more useful to the aerothermal and computational fluid dynamics (CFD) modelling communities.

A clear improvement in the present data analysis can be achieved if the experimental data is fit using the same computational tools that are used to simulate high-enthalpy test and flight environments. Such a procedure would ensure consistency in transport property approximations (i.e., diffusion coefficients) and allow for experiments in multispecies gas mixtures at pressures where gas-phase reactions operate in parallel with surface reactions. It would also enable more accurate modelling of the side-arm and sample geometries, and account for wall temperature distributions. The first steps along this path were taken recently, when the CFD code DPLR was applied to simulate concentration gradients in $O_2/O/CO/He$ gas mixtures inside the side-arm reactor.⁶⁸ DPLR⁷⁷ is a parallel multiblock finite-volume code that solves the Navier-Stokes equations including finite-rate chemistry and the effects of thermal nonequilibrium. DPLR, along with the CFD code LAURA,⁷⁸ are the main aerothermal analysis tools used by NASA for planetary entry vehicles.

On the experimental side, the two main system improvements would be a quicker and more accurate method of measuring the relative fluorescence detection sensitivities at the four PMTs, and extension of the experimentally accessible high temperature range. For the former task, the calibration scheme of Döbele and coworkers appears promising.⁷⁹⁻⁸¹ They use two-photon excitation of rare gas atoms at wavelengths very close to the excitation wavelengths for O and N atoms to generate a fluorescence volume with the similar geometric and emissive characteristics. Combined with knowledge of the filter transmission curves and PMT spectral sensitivity at the pertinent fluorescence wavelengths, the relative fluorescence detection sensitivities at the four PMTs could then be determined simply by filling the reactor with the appropriate gas (Xe for O-atom detection and Kr for N-atom detection).

Currently, the upper temperature limit for usable experimental measurements in the side-arm reactor is about 850 °C. This limit is determined by the signal-to-noise ratio in the LIF signal. LIF signals decrease with temperature for a number of reasons, including lower gas densities, greater surface loss rates and in the case of O-atoms, depletion of the $J = 2$ fine structure level population in the electronic ground state. However, in general, signal strength is not the limiting factor; rather it is the fluctuating thermal background emanating from the furnace at high temperatures that overwhelms the atom signal. This background cannot be filtered

out since it arises in the near infrared region at the same wavelengths transmitted by the narrow band filters on the PMTs.

One solution to this problem is to seek alternate excitation schemes that fluoresce in the visible range. Preliminary experiments were conducted exciting the $4p\ ^3P_{2,1,0} \leftarrow 2p\ ^3P_2$ two-photon transition at 200.6 nm. Fluorescence from the excited state via the $4p\ ^3P_{2,1,0} \rightarrow 3s\ ^3S_1^0$ transition generates light near 437 nm. At this wavelength, gas temperatures above 1200 °C can be reached before background thermal radiation levels reach comparable levels. The two-photon cross-section is a factor of four smaller and the excited state lifetime a factor of ~6 longer than in the traditional O-atom LIF scheme. Further, only ~10% of the total fluorescence is emitted at 437 nm.⁸² Nevertheless, the signal to noise ratio observed in experiments at elevated temperatures was significantly improved. Unfortunately, additional complications arise from the unintended photodissociation of vibrationally excited O₂ molecules in the Schumann-Runge bands above ~700 °C, making the ultimate utility of this scheme doubtful.

A more promising approach is to combine the present LIF schemes with on-axis fluorescence detection. Exploratory measurements demonstrate that this detection orientation eliminates almost all of the thermal background interference, since the background field of view seen by the PMT is essentially the cold exit window on the cross (Fig. 8). The trade off for this arrangement is the difficulty in achieving spatial resolution along the tube centreline, which must be done either by spatially discriminating collection optics or by bringing the excitation laser in through the side of the furnace at normal incidence to the side-arm tube.

5.0 CONCLUDING REMARKS

The experimental characterization and numerical modelling of surface reactions on TPS materials remain challenging problems. Uncertainties in the catalytic component of aeroconvective heating contribute significantly to the overall uncertainty in aerothermal heating predictions for many flight and test environments. One ramification of this situation is the default assumption of fully-catalytic surfaces in TPS sizing calculations. Another consequence is the difficulty in separating catalytic and turbulent contributions to measured heating rates in turbulent hypersonic test environments.

Improvements in our capability to incorporate robust and validated models for high temperature surface chemistry on TPS in hypersonic environments will require continued experimentation both in high-enthalpy and low-enthalpy facilities. With continuing development of experimental techniques and data analysis procedures, the diffusion tube side-arm reactor approach can be used to make useful contributions to this effort.

6.0 ACKNOWLEDGEMENTS

Many people have contributed to the work described in this lecture. The guidance and collaboration of Joan Pallix, Doug Fletcher, and Doug Bamford are gratefully acknowledged. Special thanks are due the David Stewart of NASA Ames Research Center who introduced me to the subject of surface catalysis, and to Richard Copeland of SRI International who taught me about laser diagnostics. My work in this area has been supported through NASA and AFOSR funding.

7.0 REFERENCES

- ¹ Rakich, J.V., Stewart, D.A., and Lanfranco, M.J., "Results of a Flight Experiment on the Catalytic Efficiency of the Space Shuttle Heat Shield," AIAA Paper 82-0944, 1982.
- ² Stewart, D.A., Rakich, J.V., and Lanfranco, M.J., "Catalytic Surface Effects Experiment on the Space Shuttle," AIAA Paper 81-1143, 1981.
- ³ Stewart, D.A., Rakich, J.V., and Lanfranco, M.J., "Catalytic Surface Effects on Space Shuttle Thermal Protection System during Earth Entry of Flights STS-2 through STS-5," NASA CP-2283, Hampton, VA, March 1983.
- ⁴ Masel, R.I., *Adsorption and Reaction on Solid Surfaces*, John Wiley & Sons, Inc., New York, 1996.
- ⁵ Deutschmann, O., Riedel, U., and Warnatz, J., "Modeling of Nitrogen and Oxygen Recombination on Partial Catalytic Surfaces," *Journal of Heat Transfer*, Vol. 117, 1995, pp. 495-501.
- ⁶ Jumper, E.J. and Seward, W.A., "Model of Oxygen Recombination on Reaction-Cured Glass," *Journal of Thermophysics and Heat Transfer*, Vol. 8, 1994, pp. 460-465.
- ⁷ Daiß, A., Frühauf, H.-H., and Messerschmid, E.W., "Modeling Catalytic Reactions on Silica Surfaces with Consideration of Slip Effects," *Journal of Thermophysics and Heat Transfer*, Vol. 11, 1997, pp. 346-352.
- ⁸ Natsui, F., Barbato, M., and Bruno, C., "Material-Dependent Catalytic Recombination Modeling for Hypersonic Flows," *Journal of Thermophysics and Heat Transfer*, Vol. 10, 1996, pp. 131-136.
- ⁹ Stewart, D.A., "Determination of Surface Catalytic Efficiency for Thermal Protection Materials - Room Temperature to Their Upper Use Limit," AIAA Paper 96-1863, June 1996.
- ¹⁰ Stewart, D.A., "Surface Catalysis and Characterization of Proposed Candidate TPS for Access-to-Space Vehicles," NASA TM-112206, July 1997.
- ¹¹ Stewart, D.A., "Surface Catalytic Efficiency of Advanced Carbon Carbon Candidate Thermal Protection Materials for SSTO Vehicles," NASA TM-110383, February 1996.
- ¹² Laidler, K.J., *Chemical Kinetics*, McGraw-Hill Book Company, New York, 1965.
- ¹³ Smith, W.V., "The Surface Recombination of H Atoms and OH Radicals," *Journal of Chemical Physics*, Vol. 11, 1943, pp. 110-125.
- ¹⁴ Melin, G.A. and Madix, R.J., "Energy Accommodation During Hydrogen Atom Recombination on Metal Surfaces," *Transactions of the Faraday Society*, Vol. 67, 1971, pp. 2711-2719.
- ¹⁵ Melin, G.A. and Madix, R.J., "Energy Accommodation During Oxygen Atom Recombination on Metal Surfaces," *Transactions of the Faraday Society*, Vol. 67, 1971, pp. 198-211.
- ¹⁶ Greaves, J.C. and Linnett, J.W., "Recombination of Atoms at Surfaces, Part 4 - Theory of Method and Measurement of Atom Concentrations," *Transactions of the Faraday Society*, Vol. 55, 1959, pp. 1338-1345.
- ¹⁷ Greaves, J.C. and Linnett, J.W., "Recombination of Atoms at Surfaces, Part 5 - Oxygen Atoms at Oxide Surfaces," *Transactions of the Faraday Society*, Vol. 55, 1959, pp. 1346-1354.
- ¹⁸ Greaves, J.C. and Linnett, J.W., "Recombination of Atoms at Surfaces, Part 6 - Recombination of Oxygen Atoms on Silica from 20 °C to 600 °C," *Transactions of the Faraday Society*, Vol. 55, 1959, pp. 1355-1361.
- ¹⁹ Greaves, J.C. and Linnett, J.W., "The Recombination of Oxygen Atoms at Surfaces," *Transactions of the Faraday Society*, Vol. 54, 1958, pp. 1323-1330.
- ²⁰ Linnett, J.W. and Marsden, D.G.H., "The Kinetics of the Recombination of Oxygen Atoms at a Glass Surface," *Proceedings of the Royal Society of London, A*, Vol. 234, 1956, pp. 489-504.
- ²¹ Linnett, J.W. and Rahman, M.L., "Recombination of Atoms at Surfaces, part 13 - Oxygen Atoms on $Zn_xFe_{3-x}O_4$ and $Ni_xFe_{3-x}O_4$," *Transactions of the Faraday Society*, Vol. 67, 1971, pp. 191-197.
- ²² Rahman, M.L. and Linnett, J.W., "Recombination of Atoms at Surfaces, part 10 - Nitrogen Atoms at Pyrex Surfaces," *Transactions of the Faraday Society*, Vol. 67, 1971, pp. 170-178.

- 23 Rahman, M.L. and Linnett, J.W., "Recombination of Atoms at Surfaces, part 11 - Nitrogen Atoms at
Some Acid, Base, and Salt Surfaces," *Transactions of the Faraday Society*, Vol. 67, 1971, pp. 179-
182.
- 24 Rahman, M.L. and Linnett, J.W., "Recombination of Atoms at Surfaces, part 12 - Nitrogen Atoms at
Some Metal and Alloy Surfaces," *Transactions of the Faraday Society*, Vol. 67, 1971, pp. 183-190.
- 25 Ablow, C.M., Motz, H., and Wise, H., "Diffusion and Heterogeneous Reaction. VII. Effect of
Different Catalyst Geometries," *Journal of Chemical Physics*, Vol. 43, 1965, pp. 10-14.
- 26 Ablow, C.M. and Wise, H., "Diffusion and Heterogeneous Reaction. VIII. Kinetic Considerations of
Surface Reactions," *Journal of Chemical Physics*, Vol. 46, 1967, pp. 3424-3428.
- 27 Motz, H. and Wise, H., "Diffusion and Heterogeneous Reaction. III. Atomic Recombination at a
Catalytic Boundary," *Journal of Chemical Physics*, Vol. 32, 1960, pp. 1893-1894.
- 28 Sancier, K.M., "Luminescence of Solids Excited by Surface Recombination of Atoms. V.
Quantitative Dependence of Luminescence Response on Oxygen- and Nitrogen-Atom Densities,"
Journal of Chemical Physics, Vol. 42, 1965, pp. 1240-1243.
- 29 Sancier, K.M., Fredericks, W.J., Hatchett, J.L., and Wise, H., "Luminescence of Solids Excited by
Surface Recombination of Atoms. II. Recombination Coefficients," *Journal of Chemical Physics*,
Vol. 37, 1962, pp. 860-864.
- 30 Sancier, K.M. and Wise, H., "Diffusion and Heterogeneous Reaction. XI. Diffusion Coefficient
Measurements for Gas Mixture of Atomic and Molecular Hydrogen," *Journal of Chemical Physics*,
Vol. 51, 1969, pp. 1434-1438.
- 31 Wise, H. and Ablow, C.M., "Diffusion and Heterogeneous Reaction. I. The Dynamics of Radical
Reactions," *Journal of Chemical Physics*, Vol. 29, 1958, pp. 634-639.
- 32 Wise, H. and Ablow, C.M., "Diffusion and Heterogeneous Reaction. IV. Effects of Gas-Phase
Reaction and Convective Flow," *Journal of Chemical Physics*, Vol. 35, 1961, pp. 10-18.
- 33 Wise, H., Ablow, C.M., and Sancier, K.M., "Diffusion and Heterogeneous Reaction. VI. Surface
Recombination in the Presence of Distributed Atom Sources," *Journal of Chemical Physics*, Vol. 41,
1964, pp. 3569-3573.
- 34 Wise, H., Ablow, C.M., and Schott, D.J., "Diffusion and Heterogeneous Reaction. V. Transition from
a Surface- to a Diffusion-Controlled Process during Atom Recombination," *Journal of Chemical
Physics*, Vol. 39, 1963, pp. 2063-2067.
- 35 Wise, H. and Wood, B.J., "Energy Transfer during Atom Recombination on Solid Surfaces," in
Rarefied Gas Dynamics; Vol. 1, edited by J. A. Laurmann, (Academic Press, New York, 1963), p.
470-477.
- 36 Wise, H. and Wood, B.J., "Reactive Collisions Between Gas and Surface Atoms," in *Advances in
Atomic and Molecular Physics; Vol. 3*, edited by D. R. Bates and I. Estermann, (Academic Press, New
York, 1967), p. 291-353.
- 37 Wood, B.J. and Wise, H., "Diffusion and Heterogeneous Reaction. II. Catalytic Activity of Solids for
Hydrogen-Atom Recombination," *Journal of Chemical Physics*, Vol. 29, 1958, pp. 1416-1417.
- 38 Wood, B.J. and Wise, H., "The Interaction of Atoms with Solid Surfaces," in *Rarefied Gas Dynamics*,
edited by L. Talbot, (Academic Press, New York, 1961), p. 51-59.
- 39 Wood, B.J. and Wise, H., "The Kinetics of Hydrogen Atom Recombination on Pyrex Glass and Fused
Quartz," *Journal of Physical Chemistry*, Vol. 66, 1962, pp. 1049-1053.
- 40 Wood, B.J. and Wise, H., "Kinetics of Hydrogen Atom Recombination on Surfaces," *Journal of
Physical Chemistry*, Vol. 65, 1961, pp. 1976-1983.
- 41 Kaufman, F., "Reactions of Oxygen Atoms," in *Progress in Reaction Kinetics; Vol. 1*, edited by C.
Porter, (Pergamon Press, 1961), p. 3-39.
- 42 Marshall, T., "Surface Recombination of Nitrogen Atoms Upon Quartz," *Journal of Chemical
Physics*, Vol. 37, 1962, pp. 2501-2502.

- 43 Marshall, T.C., "Studies of Atomic Recombination of Nitrogen, Hydrogen, and Oxygen by
44 Paramagnetic Resonance," *Physics of Fluids*, Vol. 5, 1962, pp. 743-753.
- 45 Evenson, K.M. and Burch, D.S., "Atomic-Nitrogen Recombination," *Journal of Chemical Physics*,
46 Vol. 45, 1966, pp. 2450-2460.
- 47 Kim, Y.C. and Boudart, M., "Recombination of O, N, and H Atoms on Silica: Kinetics and
48 Mechanism," *Langmuir*, Vol. 7, 1991, pp. 2999-3005.
- 49 Brennan, D., "Heterogeneous Atomisation and Recombination," in *Comprehensive Chemical Kinetics*.
50 *Volume 21, Reactions of Solids with Gases*, edited by C. H. Bamford, C. E. H. Tripper, and R. G.
51 Compton, (Elsevier, New York, 1984), p. 151-231.
- 52 Balat, M., Czerniak, M., and Badie, J.M., "Thermal and Chemical Approaches for Oxygen Catalytic
53 Recombination Evaluation on Ceramic Materials at High Temperature," *Applied Surface Science*,
54 Vol. 120, 1997, pp. 225-238.
- 55 Balat-Pichelin, M., Badie, J.M., Berjoan, R., and Boubert, P., "Recombination Coefficient of Atomic
56 Oxygen on Ceramic Materials Under Earth Re-Entry Conditions by Optical Emission Spectroscopy,"
57 *Chemical Physics*, Vol. 291, 2003, pp. 181-194.
- 58 Balat-Pichelin, M. and Duqueroie, F., "Heat Transfer Modeling at High Temperature for the
59 Evaluation of Atomic Oxygen Recombination Energy on Ceramic Materials," *International Journal*
60 *of Thermal Sciences*, Vol. 40, 2001, pp. 279-287.
- Bedra, L. and Balat-Pichelin, M., "Comparative Modeling Study and Experimental Results of Atomic
Oxygen Recombination on Silica-Based Surfaces at High-Temperature," *Aerospace Science and*
Technology, Vol. 9, 2005, pp. 318-328.
- Booth, J.P., Joubert, O., Pelletier, J., and Sadeghi, N., "Oxygen Atom Actinometry Reinvestigated:
Comparisons with Absolute Measurements by Resonance Absorption at 130 nm," *Journal of Applied*
Physics, Vol. 69, 1991, pp. 618-626.
- Katsch, H.M., Tewes, A., Quandt, E., Goehlich, A., Kawetzki, T., and Döbele, H.F., "Detection of
Atomic Oxygen: Improvement of Actinometry and Comparison with Laser Spectroscopy," *Journal of*
Applied Physics, Vol. 88, 2000, pp. 6232-6238.
- Guyon, C., Cavadias, S., and Amouroux, J., "Heat and Mass Transfer Phenomenon from an Oxygen
Plasma to a Semiconductor Surface," *Surface and Coating Technology*, Vol. 142-144, 2001, pp. 959-
963.
- Guyon, C., Cavadias, S., Mabilie, I., Moscossa-Santillan, M., and Amouroux, J., "Recombination of
Oxygen Atomic Excited States Produced by Non-Equilibrium RF Plasma on Different Semiconductor
Materials: Catalytic Phenomena and Modelling," *Catalysis Today*, Vol. 89, 2004, pp. 159-167.
- Cauquot, P., Cavadias, S., and Amouroux, J., "Thermal Energy Accommodation from Oxygen Atoms
Recombination on Metallic Surfaces," *Journal of Thermophysics and Heat Transfer*, Vol. 12, 1998,
pp. 206-213.
- Mozetič, M., Drobnič, M., and Zalar, A., "Recombination of Neutral Hydrogen Atoms on AISI 304
Stainless Steel Surface," *Applied Surface Science*, Vol. 144-145, 1999, pp. 399-403.
- Mozetič, M. and Zalar, A., "Recombination of Neutral Oxygen Atoms on Stainless Steel Surface,"
Applied Surface Science, Vol. 158, 2000, pp. 263-267.
- Mozetič, M., Zalar, A., Cvelbar, U., and Poberaj, I., "Heterogeneous Recombination of Neutral
Oxygen Atoms on Niobium Surface," *Applied Surface Science*, Vol. 211, 2003, pp. 96-101.
- Pallix, J.B. and Copeland, R.A., "Measurement of Catalytic Recombination Coefficients on Quartz
Using Laser-Induced Fluorescence," *Journal of Thermophysics and Heat Transfer*, Vol. 10, 1996, pp.
224-233.
- Marschall, J., "Experimental Determination of Oxygen and Nitrogen Recombination Coefficients at
Elevated Temperature Using Laser-Induced Fluorescence," AIAA Paper 97-3879, August 1997.

- 61 Bischel, W.K., Perry, B.E., and Crosley, D.R., "Two-Photon Laser-Induced Fluorescence in Oxygen
and Nitrogen Atoms," *Chemical Physics Letters*, Vol. 82, 1981, pp. 85-88.
- 62 Bischel, W.K., Perry, B.E., and Crosley, D.R., "Detection of Fluorescence from O and N Atoms
Induced by Two-Photon Absorption," *Applied Optics*, Vol. 21, 1982, pp. 1419-1428.
- 63 Adams, S.F. and Miller, T.A., "Two-Photon Absorption Laser Induced Fluorescence of Atomic
Nitrogen by an Alternative Excitation Scheme," *Chemical Physics Letters*, Vol. 295, 1998, pp. 305-
311.
- 64 Bashkin, S. and Stoner, J.O., Jr., *Atomic Energy Levels and Grotrian Diagrams*, Vol. 1 Elsevier
Publishing Company, Inc., New York, 1975.
- 65 Dagdigan, P.J., Forch, B.E., and Miziolek, A.W., "Collisional Transfer Between and Quenching of
the $3p^3P$ and $5P$ States of the Oxygen Atom," *Chemical Physics Letters*, Vol. 148, 1988, pp. 299-308.
- 66 Copeland, R.A., Jeffries, J.B., Hickman, A.P., and Crosley, D.R., "Radiative Lifetime and Quenching
of the $3p^4D^o$ State of Atomic Nitrogen," *Journal of Chemical Physics*, Vol. 86, 1987, pp. 4876-4884.
- 67 Jeffries, J.B., Copeland, R.A., and Crosley, D.R., "Intermultiplet Energy Transfer in the Collisions of
 $3p^4D^o$ Nitrogen Atoms with Nitrogen Molecules," *Journal of Chemical Physics*, Vol. 91, 1989, pp.
2200-2205.
- 68 Marschall, J., Copeland, R.A., Hwang, H.H., and Wright, M.J., "Surface Catalysis Experiments on
Metal Surfaces in Oxygen and Carbon Monoxide Mixtures," AIAA Paper 2006-181, January 2006.
- 69 Berkowitz, J., "Catalytic Oxygen Atom Recombination on Solid Surfaces," in *The Structure and
Chemistry of Solid Surfaces*, edited by G. A. Somorjai, (John Wiley & Sons, Inc., New York, 1968),
p. 80.81-80.16.
- 70 Dickens, P.G. and Sutcliffe, M.B., "Recombination of Oxygen Atoms on Oxide Surfaces,"
Transactions of the Faraday Society, Vol. 60, 1964, pp. 1272-1285.
- 71 Hartunian, R.A., Thompson, W.P., and Safron, S., "Measurement of Catalytic Efficiency of Silver for
Oxygen Atoms and the O-O₂ Diffusion Coefficient," *Journal of Chemical Physics*, Vol. 43, 1965, pp.
4003-4006.
- 72 Myerson, A.L., "Exposure-Dependent Surface Recombination Efficiencies of Atomic Oxygen,"
Journal of Chemical Physics, Vol. 50, 1969, pp. 1228-1234.
- 73 Marschall, J., Chamberlain, A., Crunkleton, D., and Rogers, B., "Catalytic Atom Recombination on
ZrB₂/SiC and HfB₂/SiC Ultra-High Temperature Ceramic Composites," *Journal of Spacecraft and
Rockets*, Vol. 41, 2004, pp. 576-581.
- 74 Copeland, R.A., Pallix, J.B., and Stewart, D.A., "Surface Catalyzed Production of NO From
Recombination of N and O Atoms," *Journal of Thermophysics and Heat Transfer*, Vol. 12, 1998, pp.
496-499.
- 75 Kurotaki, T., "Catalytic Model on SiO₂-Based Surface and Application to Real Trajectory," *Journal of
Spacecraft and Rockets*, Vol. 38, 2001, pp. 798-800.
- 76 Sepka, S., Chen, Y.-K., Marschall, J., and Copeland, R.A., "Experimental Investigation of Surface
Reactions in Carbon Monoxide and Oxygen Mixtures," *Journal of Thermophysics and Heat Transfer*,
Vol. 14, 2000, pp. 45-52.
- 77 Wright, M.J., Candler, G.V., and Bose, D., "Data-Parallel Line Relaxation Method for the Navier-
Stokes Equations," *AIAA Journal*, Vol. 36, 1998, pp. 1603-1609.
- 78 Cheatwood, F.M. and Gnoffo, P.A., "User's Manual for the Langley Aerothermodynamic Upwind
Relaxation Algorithm (LAURA)," NASA TM-4764, April 1996.
- 79 Niemi, K., Gathen, V.S.-v.d., and Döbele, H.F., "Absolute Atomic Oxygen Density Measurements by
Two-Photon Absorption Laser-Induced Fluorescence Spectroscopy in an RF-Excited Atmospheric
Pressure Plasma Jet," *Plasma Sources Science and Technology*, Vol. 14, 2005, pp. 375-386.

- ⁸⁰ Niemi, K., Gathen, V.S.-v.d., and Döbele, H.F., "Absolute Calibration of Atomic Density Measurements by Laser-Induced Fluorescence Spectroscopy with Two-Photon Excitation," *Journal of Physics D: Applied Physics*, Vol. 34, 2001, pp. 2330-2335.
- ⁸¹ Goehlich, A., Kawetzki, T., and Döbele, H.F., "On Absolute Calibration with Xenon of Laser Diagnostic Methods Based on Two-Photon Absorption," *Journal of Chemical Physics*, Vol. 108, 1998, pp. 9362-9370.
- ⁸² Bamford, D.J., Saxon, R.P., Jusinski, L.E., Buck, J.D., and Bischel, W.K., "Two-Photon Excitation of Atomic Oxygen at 200.6, 192.5, and 194.2 nm: Absolute Cross Sections and Collisional Ionization Rate Constants," *Physical Review A*, Vol. 37, 1988, pp. 3259-3269.